Amygdalostriatal transition zone neurons encode sustained valence to direct conditioned behaviors

Fergil Mills [1,*], Christopher R. Lee [1,2,*], James R. Howe [2,*], Hao Li [1,*], Shan Shao [3], Maria N. Keisler [1,4], Mackenzie E. Lemieux [1], Felix H. Taschbach [1,2], Laurel R. Keyes [1,4], Matilde Borio [1], Hannah S. Chen [5], Reesha R. Patel [1], Alexa L. Gross [6], Jeremy Delahanty [1], Christian Cazares [1], Liezl Maree [1], Romy Wichmann [1], Talmo D. Pereira [1], Marcus K. Benna [2], Cory M. Root [2], and Kay M. Tye [1,2,4,7].

1 Salk Institute for Biological Studies, La Jolla, CA, USA

2 University of California San Diego, La Jolla, CA, USA

3 Peking University, Beijing, China

4 Howard Hughes Medical Institute, La Jolla, CA, USA

5 MIT, Cambridge, MA, USA

6 Wellesley College, Wellesley, MA, USA

7 Kavli Institute for the Brain and Mind, La Jolla, CA, USA

*** These authors contributed equally**

To Whom Correspondence Should be Addressed:

Kay M. Tye, PhD
HHMI Investigator
Wylie Vale Professor, Salk Institute for Biological Studies
10010 North Torrey Pines Road, La Jolla, CA 92037, USA.
tye@salk.edu
@kaymtye

SUMMARY

In order to respond appropriately to threats in the environment, the brain must rapidly determine whether a stimulus is important and whether it is positive or negative, and then use that information to direct behavioral responses. Neurons in the amygdala have long been implicated in valence encoding and in fear responses to threatening stimuli, but show transient firing responses in response to these stimuli that do not match the timescales of associated behavioral responses. For decades, there has been a logical gap in how behavioral responses could be mediated without an ensemble representation of the internal state of valence that has rapid onset, high signal-to-noise, and is sustained for the duration of the behavioral state. Here, we present the amygdalostriatal transition zone (ASt) as a missing piece of this highly conserved process that is of paramount importance for survival, which does exactly this: represents an internal state (e.g. fear) that can be expressed in multiple motor outputs (e.g. freezing or escape). The ASt is anatomically positioned as a “shortcut” to connect the corticolimbic system (important for evaluation) with the basal ganglia (important for action selection) with the inputs of the amygdala and the outputs of the striatum – ideally poised for evaluating and responding to environmental threats. From *in vivo* cellular resolution recordings that include both electrophysiology and calcium imaging, we find that ASt neurons are unique in that they are sparse coding, extremely high signal-to-noise, and also maintain a sustained response for negative valence stimuli for the duration of the defensive behavior – a rare but essential combination. We further show that photostimulation of the ASt is sufficient to drive freezing and avoidance behaviors. Using single-nucleus RNA sequencing and *in situ* RNA labelling we generate a comprehensive profile of cell types and gene expression in the ASt, and find the ASt is genetically distinct from adjacent striatal and amygdalar structures. We also find that the ASt has a greater proportion of neurons expressing *Drd2* than neurons expressing *Drd1a*, a unique feature compared to other regions of the striatum. Using *in vivo* calcium imaging, we show that that this *Drd2*+ population robustly encodes stimuli of negative valence, and in loss-of-function experiments find that optogenetic inhibition of *Drd2*+ ASt neurons causes a striking reduction in cue-conditioned fear responses. Together, our findings identify the ASt as a previously-unappreciated critical missing link for encoding learned associations and directing ongoing behavior.

INTRODUCTION

Associative learning is critical for survival and is necessary to direct appropriate behavioral responses to environmental stimuli that predict rewards or punishments. However, appetitive and aversive behaviors are inherently distinct. Appetitive behaviors such as hunting, foraging, and mating are generally self-initiated motor sequences that may or may not be time-locked to the presentation of a reward-predictive stimulus. In contrast, for effective defensive and escape behaviors environmental stimuli must trigger an immediate response; to respond appropriately, we need to select important information, assign valence, select an action, and execute that action for the duration of the threat.

For decades, the amygdala has been studied as a key structure for orchestrating defensive fear responses, and shown to be a critical site for encoding learned associations of both positive and negative valence (Gallagher and Holland, 1994; Jennings et al., 2013; Josselyn et al., 2015; Kim et al., 2016; Kong and Zweifel, 2021; LeDoux, 1992; Marcinkiewcz et al., 2016; Maren, 2005; Piantadosi et al., 2022; Quirk et al., 1995; Tye, 2018; Weiskrantz, 1956). In particular, the central nucleus of the amygdala (CeA) and its outputs play a key role in conditioned fear responses and mediate freezing and escape behaviors (Ciocchi et al., 2010; Fadok et al., 2017; Haubensak et al., 2010; Keifer et al., 2015; LeDoux et al., 1988; Tovote et al., 2016).

However, an unresolved mystery in current models of amygdala function is the discrepancy in timescales between the activity of amygdala complex neurons and the conditioned behaviors that they drive. Neurons in the amygdala exhibit increased responses to a conditioned stimulus (CS), but these are often only transient, lasting less than a second from the onset of a sensory stimulus (Goosens and Maren, 2004; Li et al., 2022; Quirk et al., 1995, 1995; Tye et al., 2008; Whittle et al., 2021). This does not match the behaviors that can be elicited by these stimuli, which include defensive responses expressed for the full duration of the threat presentation that would be essential to survive or evade threats in the real world. Mediating these behaviors would ideally require a neural substrate which is connected to circuits for learning and valence processing, can rapidly respond to stimuli, and is upstream of circuits able to direct appropriate behaviors.

A structure which is well-situated to play a role in these processes is the woefully understudied amygdalostriatal transition zone (ASt). The function of the ASt in encoding valence and directing behavior is currently unknown and represents a major gap in our understanding of circuits mediating motivated behaviors. However, the limited data collected of ASt neuron activity shows that the ASt receives the necessary information to encode learned associations. For instance, single-unit recordings indicate that ASt neurons respond to auditory, visual and somatosensory stimuli, including painful stimuli such as foot shocks (Romanski et al., 1993; Uwano et al., 1995). ASt responses to stimuli are fast, with lower latency than responses in the basolateral amygdala (BLA) or CeA, and of similar latency to responses in the lateral amygdala (LA) (Bordi et al., 1993; Quirk et al., 1995; Uwano et al., 1995). Indeed, like the LA, the ASt receives converging inputs from thalamic and cortical pathways, including calretinin-expressing thalamic neurons that are known to relay sensory information critical for learned associations (Barsy et al., 2020). There also exists a robust direct projection from the LA to the ASt (Jolkkonen et al., 2001; Wang et al., 2002). The LA is known to be a key site for emotional memory formation (Blair et al., 2001; Fanselow and LeDoux, 1999; Maren, 2005; Maren and Quirk, 2004; Sah et al., 2008), and the existence of this direct LA input to the ASt is intriguing as propagation of signals from the LA to ASt is even more rapid than from the LA to the BLA (Wang et al., 2002). This suggests that information about learned associations encoded in the LA may be rapidly routed to the ASt to mediate components of conditioned responses to stimuli.

Together, these studies show that the ASt can rapidly respond to stimuli and is connected with known amygdala circuits for emotional learning and valence processing. However, the outputs of the ASt diverge significantly from the amygdala complex, and are integrated with striatal pathways known to control action selection and execution. ASt neurons project to the globus pallidus and substantia nigra pars lateralis (Jolkkonen et al., 2001; Shammah-Lagnado et al., 1999), which are both major target structures of the ‘direct’

and 'indirect' striatal pathways characterized by the respective expression of dopamine receptor 1 (*Drd1a*) and dopamine receptor 2 (*Drd2*) in striatal medium spiny neurons (MSNs) (Gerfen et al., 1990; Nelson and Kreitzer, 2014). The direct and indirect pathways have been shown to mediate opposing and complementary effects on action selection and motor output (Cui et al., 2013; Kravitz et al., 2012, 2010; Markowitz et al., 2018; Nelson and Kreitzer, 2014; Tai et al., 2012). Thus, the outputs of the ASt are well-situated to mediate the selection and expression of specific behaviors guided by learned valence assignment. This positions the ASt at a crucial intersection of systems in the brain, bridging corticolimbic circuits involved in the recognition and learning of threats with basal ganglia circuits responsible for selection and execution of actions.

To establish the ASt's unique functional role and to distinguish it from other well-studied structures of complementary function, we perform a systematic comparison spanning *systems* (large-scale ensemble dynamics), *circuit* (cell-type specific dynamics and manipulations), and *molecular* (transcriptomic profiling) levels of investigation across three neighboring regions of similar composition. We perform high-density electrophysiological recordings in the ASt and the adjacent CeA and tail of striatum (TS), and find that ASt neurons show robust sustained responses to cues of negative valence across behaviorally-relevant time scales, and that activation of ASt neurons is sufficient to drive robust freezing and avoidance behaviors. We also characterize the cell types and gene expression in the ASt and surrounding structures using single-nucleus RNA sequencing, and find that the ASt is a genetically distinct region with a significantly greater proportion of *Drd2*+ neurons than other regions of the striatum. Finally, we show that *Drd2*+ ASt neurons encode stimuli of negative valence and are critical for expression of cue-conditioned fear responses, but not reward responses or contextual fear. Together, these findings identify the ASt as a novel structure of interest for associative learning and as a critical missing piece of the neural mechanisms for expression of motivated behaviors.

RESULTS:

The ASt Encodes Conditioned Stimuli

The ASt is extensively interconnected with circuits known to be involved in associative learning (**Figure 1A**), and we first sought to determine whether ASt neurons were involved in the encoding of conditioned responses to stimuli of positive and negative valence. We began by recording the endogenous activity of ASt neurons in freely-moving mice using chronically implanted probes for *in vivo* electrophysiology (**Figure 1B, S1A-C**). ASt neuron activity was examined in a two-tone discrimination task, where a pair of distinct pure tones (20s in length, 3.5 kHz and 20 kHz, counterbalanced for each conditioned stimulus (CS) type within all groups) predicted either an aversive footshock (100 ms, 0.7 mA) or delivery of a reward (7.5 µL chocolate Ensure™) to a reward port in the test apparatus. Mice were trained on this task until they showed robust defensive behaviors in response to CS-shock and port entry responses to CS-reward (**Figure S1D-F**). The behavioral discrimination between the two tones indicated the mice had successfully learned the contingencies of each CS-type, allowing us to examine their neural activity for encoding of the learned associations and conditioned behaviors. To distinguish between responses of neurons to sensory stimuli and conditioned responses driven by associative learning, we also examined neural responses to stimuli in 'unpaired' control group mice, who received the same tone and US presentations but in randomized order and explicitly unpaired so the tones had no predictive significance.

Our recording probes targeting the ASt also recorded neuronal responses from the adjacent regions, the tail of the striatum (TS) and central nucleus of the amygdala (CeA), both predominantly GABAergic regions which lie immediately dorsal and ventral, respectively, to the ASt (**Figure 1A**). This allowed us to record conditioned responses to CS-shock and CS-reward in these structures simultaneously during the same task, and compare them to those of the ASt. We began by examining recorded neurons from all regions together, using hierarchical clustering to group neurons based on their response profiles to each CS type (**Figure 1D**). Neurons from the ASt, TS and CeA showed considerable heterogeneity in responses to stimuli of positive and negative valence, and we examined the average responses and the representation of neurons from each region within each functional cluster (**Figure 1E**). Neurons from the CeA and ASt formed a relatively greater proportion of neurons which had transient responses to CS-shock and CS-reward (Cluster 3), while neurons from the TS were the greatest relative proportion of neurons which showed inhibitory responses to CS reward (Clusters 2 and 9). However, ASt neurons were the dominant representative in one of the most highly responsive clusters (Cluster 1), a functional cluster of neurons which showed minimal responses to CS-reward, but robust and sustained responses to CS-shock.

We then examined each individual region's overall neural responses to stimuli of positive and negative valence (**Figure 2A-C**). Our recordings revealed that ASt neurons, on a population level, showed conditioned responses to CS-shock and CS-reward cues, a previously unknown role for this structure (**Figure 2A**). To further characterize encoding of these cues across regions, we examined trial-averaged trajectories of neuron population activity in the ASt, TS and CeA during presentation of each CS (**Figure 2D-F, Supplementary Video 1-3**) (Allsop et al., 2018; Cunningham and Yu, 2014; Glaser et al., 2020; Padilla-Coreano et al., 2022). In paired group mice, ASt neuron trajectories during CS-shock and CS-reward moved in orthogonal directions from the time of cue onset, with CS-shock trajectories maintaining distance from the baseline position throughout the entire CS. The divergent paths of the trajectories indicate that, even during the transient period where ASt neurons respond to both CS-shock and CS-reward, the population distinctly encoded the two stimuli of opposing valences despite the apparent similarity in the perievent time histograms (**Figure 2A**). To quantify the responses in each region, we examined phasic (1-100 ms) and sustained (100 ms – 18s) response windows after cue onset to both CS-shock and CS-reward in the ASt, TS and CeA, and compared responses during these time periods between paired and unpaired group mice (**Figure 2G-I**). We found that the ASt had robust phasic responses to stimuli of positive and negative valence and sustained responses to CS-shock, all

of which were only seen in paired group mice and absent in unpaired controls (**Figure 2G**). TS neurons showed no significant phasic responses to CS-shock, but some gradually increasing sustained responses, and phasic excitatory responses to CS-reward, but inhibitory responses during the sustained period (**Figure 2H**). In contrast, the CeA had robust phasic responses to both CS types but no significant sustained responses. Finally, we directly compared the magnitude of conditioned responses in paired group mice from neurons in each region (**Figure 2J**). ASt neurons showed robust phasic responses to both CS-shock and CS-reward that were of comparable magnitude to responses in the CeA but significantly greater than phasic responses in the TS (**Figure 2K**). However, ASt neurons showed significantly greater magnitude of sustained responses to CS-shock than either the TS or CeA. Thus, while each examined region had a unique pattern of response profiles to each CS type, the sustained responses to negative-valence stimuli was a major feature differentiating neural responses in the ASt from adjacent structures.

ASt Neuron Activity is Sufficient to Drive Freezing and Avoidance Behavior

Given that ASt neurons respond to stimuli predicting shocks and rewards, we then sought to determine what behaviors might be driven by activation of ASt neurons. To investigate this, we targeted expression of channelrhodopsin-2 (ChR2) to the ASt using a Cre-conditional viral construct in *VGAT-Cre* mice (**Figure 3A, S2A**). This approach restricted ChR2 expression to GABAergic ASt neurons in order to prevent any confounding behavioral effects caused by ChR2 in excitatory neurons in the adjacent lateral amygdala (Johansen et al., 2010; Tye et al., 2011). We then examined the effects of optogenetic activation of ASt neurons by stimulation via an implanted optic fiber. We first found that photostimulation of ASt neurons (473nm, 5 mw, 20 Hz) in ChR2-expressing mice led to a striking increase in freezing during 'laser ON' epochs of an open field test of exploratory behavior and locomotion (**Figure 3B**). This effect was reversible, with freezing levels restored during 'laser OFF' epochs, and photostimulation had no effect in eYFP-expressing controls.

We then examined whether activation of ASt neurons was innately rewarding or aversive using a closed-loop real-time place preference task, wherein mice were allowed to freely explore a test apparatus in which one side was paired with optogenetic stimulation. We found that over the course of the task, mice spent less time in the 'laser ON' side, indicating that activation of ASt neurons was aversive and led to avoidance of the side paired with stimulation (**Figure 3C**). We also found that activation of ASt neurons did not lead to any change in overall anxiety-related behaviors such as preference for the center of the open field arena (**Figure S2B**) and preference for open arms of an elevated plus maze task (**Figure S2C**). Together, these data indicated that activation of ASt neurons was innately aversive and sufficient to drive defensive freezing and avoidance behaviors, consistent with a role for the ASt in encoding fearful or aversive stimuli to direct behavioral responses.

ASt Neuron Activity Does Not Encode Specific Subsecond Motor Actions

Having seen the robust freezing elicited by ASt neuron activity, we then wondered whether the ASt represented emotional valence (internal state) or behavioral expression (motor output). The increased activity of ASt neurons during CS-shock observed in our electrophysiology experiments could be due to ASt encoding the valence of the tone, or it could be due to ASt neuron activity correlating with specific defensive behaviors – such as freezing and escape behavior – which take place in response to the CS. To distinguish between these possibilities, we re-examined our electrophysiology experiment data using SLEAP, a deep-learning based suite for pose estimation (Pereira et al., 2022), and classified behavior of individual mice during our discrimination task experiments to detect freezing and escape (rapid darting) behaviors (**Figure 3D**). Examination of individual trials (**Figure 3E,** see also **Figure S2D**) showed that ASt neuron activity increased in a manner which tracked the CS-shock in paired group mice, and while defensive behaviors also increased during that time period, specific behaviors were not closely correlated with sub-second changes in ASt neuron activity. We

identified all bouts of freezing and escape behavior during all trials of the task and found no net relative changes in ASt neuronal activity in response to onsets of either type of motor response (**Figure 3F**). Furthermore, we analyzed ASt neuron activity using logistic regression (Glaser et al., 2020) and found that during presentation of cues decoding of CS-shock was above chance level in paired group mice, but not unpaired controls, and decoding of freezing and dash behavior was not above chance level in either group (**Figure 3G**). Together, these data support the notion that the ASt represents ongoing emotional valence, as the signal is sustained throughout the cue and throughout the period of increased defensive behaviors. However, because the ASt did not show increased activity when shifting behavioral motifs and did not show phasic changes upon the initiation of freezing nor escape, we concluded that the ASt does not mediate differences in defensive strategy or motor output.

ASt Displays Unique Cell Type Composition and Transcriptomic Features Allowing Distinction From Other Striatal Regions

Given that the ASt has unique functional properties and connectivity, we next investigated the degree to which the ASt was in fact a genetically distinct brain region from adjacent structures in the striatum and amygdala. We performed single-nucleus RNA sequencing (snRNA-seq) (Zheng et al., 2017) to determine the cell type composition and transcriptomic identity of the ASt. Due to the ASt's proximity to both the striatum and amygdala complex, we extracted tissue target samples by microdissection and verified accurate histology before pooling qualifying samples for each run of RNA sequencing (see methods; **Figure 4A, S3A-F**). We also captured nuclei from the central amygdala (CeA), dorsal striatum (DS), and tail of striatum (TS) to identify differences in gene expression between these regions and the ASt (**Figure S3G-I**).

Visualization of these nuclei via uniform manifold approximation projection (UMAP) showed cluster of nuclei based on cell type, but significant divergence by region of tissue origin, with ASt cells being visibly distinct from other regions in some clusters (**Figure 4B,C**). Intriguingly, this variation occurred in a manner similar to the anatomical structure of brain, with regions spatially ordered in high-dimensional expression space based on their relative proximity to one another (DS > TS > ASt > CeA). We also confirmed there were no region-specific differences in expression of genetic markers for broad nuclear quality (Hicks et al., 2018) (**Figure S3J,K**), and both principal component analysis and hierarchical clustering of pseudobulk batches showed high variation between regions but not between batches within each region (**Figure S3L-N**), indicating that the variation observed reflected real biological differences between these regions and not other confounding methodological factors.

Clustering of sequenced nuclei by gene expression allowed us to identify all major canonical cell types in the ASt, TS, DS and CeA based on known gene markers identified in prior scRNA-seq studies of the striatum (Märtin et al., 2019; Saunders et al., 2018; Stanley et al., 2020). Across these four regions the majority of neurons fell broadly into two clusters of medium spiny neuron (MSN) defined by expression of the genes for dopamine receptor 1 (*Drd1a*) and dopamine receptor 2 (*Drd2)* (**Figures 4C-D**). We then further analyzed the various clusters of cells detected in all regions and used these to construct population analyses of relative proportions of cell types in each region and how the cell type composition of the ASt was distinct from the CeA, TS and DS (**Figure 4E-G**). Interestingly, in the ASt we saw a larger proportion of GABAergic *Drd2*+ neurons relative to other regions. To quantify this difference, we examined neurons within the *Drd1a*+ and *Drd2*+ clusters, where ASt neurons were clearly visible as a distinct subcluster from other regions (**Figure 4H-I**). In previous studies of the striatum, *Drd1a*+ and *Drd2*+ MSNs have been found to comprise the largest subpopulations of neurons, with a roughly equivalent proportion of the two types (Gagnon et al., 2017; Ren et al., 2017). We therefore quantified the overall number of neurons in the ASt in each cluster and compared this with the proportions from the DS and TS (**Figure 4J**). Our data confirmed that while both DS and TS had similar proportions of the two MSN types, the ASt was enriched for *Drd2*+ MSNs. To confirm these findings

and validate our RNAseq data, we used RNAscope labelling to examine the expression of D1 and D2 receptors *in situ* in the ASt and surrounding regions (**Figure 4K**). We found that the ASt had a much greater proportion of RNAscope-labelled *Drd2*+ neurons than *Drd1a*+ neurons compared to either the TS or DS (**Figure 4L**), and that the proportions of *Drd1a*+ and *Drd2*+ neurons in the ASt, TS and DS was highly consistent with the proportions of these cell types seen in our sequencing data (**Figure 4J**). Consistent with previous studies, we saw that in the TS, MSNs types were spatially segregated into a D1-rich medial band and a D2-rich lateral band (**Figure 4K**), but that this stratified pattern was not present in the DS or ASt (Gangarossa et al., 2013; Miyamoto et al., 2019, 2018). Furthermore, our RNAscope labelling indicated that *Drd1a*/*Drd2* dual-expressing neurons were a small proportion of the total populations in the ASt and other striatal subregions. Together, our data identify a previously unknown disparity in MSN ratio for the ASt compared to the rest of the striatum, showing that the ASt is greatly enriched for *Drd2*+ MSNs compared with other regions of the striatum.

We further examined differences in gene expression between the ASt and other structures within cell types, and found that in pairwise comparisons, ASt neurons had large numbers of differentially expressed genes compared to every other region within the *Drd1a*+ and *Drd2*+ clusters (**Figure S4**) Additionally, other striatal subregions displayed similarly diverse transcriptomic differences related to neurological function (**Figure S5B**). Taken together, these numerous differences indicate major molecular diversity among MSNs from different striatal and regions, and further indicate that ASt neurons are molecularly distinct from the rest of the striatum.

D2+ ASt neurons specifically encode conditioned stimuli of negative valence

Within the dorsal and ventral striatum, *Drd1a*+ and *Drd2*+ neurons are the two major types of GABAergic MSNs (Gagnon et al., 2017; Gangarossa et al., 2013; Gerfen et al., 1990; Gerfen and Surmeier, 2011; Ren et al., 2017). In the dorsal striatum, *Drd1*+ MSNs promote movement and reinforcement while D2-expressing cells decrease motor output and promote aversion (Kravitz et al., 2012, 2010). These motoric components are not expressed in the nucleus accumbens (NAc), wherein *Drd1*+ MSNs promote reinforcement while *Drd2*+ MSNs promote aversion (Lobo et al., 2010). These two cell types also define the direct and indirect pathways from the dorsal striatum, which have been shown to play a wide array of critical complementary and opposing roles in motor output, action selection, and control of goal-directed and habitual behaviors (Balleine and O'Doherty, 2010; Kravitz et al., 2012, 2010; Nelson and Kreitzer, 2014; Redgrave et al., 2010; Tai et al., 2012). Given the established importance of these two cell types in motor output and motivated behaviors, the heterogeneity of responses observed in ASt neuron responses in our electrophysiology experiments, and the unique increase in *Drd2*+ MSNs revealed by our RNA sequencing data, we next sought to determine the specific contributions of *Drd1a*+ and *Drd2*+ neurons in encoding conditioned stimuli in the ASt. We targeted a viral vector to the ASt of *Drd1a-Cre* and *Drd2-Cre* mice (Gong et al., 2007) to conditionally express GCaMP7f in *Drd1a*+ and *Drd2*+ ASt neurons and implanted a gradient-index relay lens immediately above the ASt to allow *in vivo* imaging of calcium transients in ASt neurons via a head-mounted miniature microscope (**Figure 5A,B, S6A-B**). We then examined calcium responses in these mice during a two-tone discrimination task (**Figure 5C**) in which distinct conditioned stimuli predicted shock ('CS-shock') and reward ('CS-reward'). Paired group mice showed evidence of discrimination, as reflected by significantly different port entry and defensive behaviors (freezing and escape) to the two cues, while no significant behavioral discrimination was seen in unpaired controls (**Figure S6C-H**).

We found that *Drd1a*+ ASt neurons overall did not show robust responses to either cue (**Figure 5D, E**), though individual neurons did show increases or decreases in activity in response to CS-reward. However, *Drd2*+ ASt neurons showed highly robust responses to CS-shock (**Figure 5F**). These responses were only seen in paired group mice, and not unpaired controls for whom the tones had no predictive value, consistent with encoding the significance of the cue of negative valence. *Drd2*+ ASt neurons showed minimal responses

to CS-reward, and group average responses to this CS in paired group mice were not significantly different than unpaired controls (**Figure 5G**). We also found that upon presentation of either shock and reward unconditioned stimulus (US) alone, subsets of *Drd1a*+ and *Drd2*+ neurons responded to each US type, with more robust responses to shocks (**Figure S7**).

To further characterize the responses of *Drd1a*+ and *Drd2*+ ASt neurons to cues of positive and negative valence, we performed additional agglomerative hierarchical clustering to identify groups of neurons based on their response patterns to each CS (**Figure 5H**). We then examined the average responses to CS-shock and CS-reward of neurons in each cluster, as well as the proportion of cells in each cluster that came from *Drd1a*+ and *Drd2*+ paired and unpaired groups (**Figure 5I**). We first saw three major clusters of cells that showed minimal responses to CS-reward and distinct but robust types of responses to CS-shock; high-amplitude (20+ Z-score) and sustained responses lasting the duration of the 10s cue (Cluster 1), transient responses to the tone onset (Cluster 2), and a gradual ramp up of activity during the CS (Cluster 3). These clusters were almost entirely composed of neurons from the *Drd2*+ paired group, and, overall, 54% of *Drd2*+ ASt neurons were clustered in one of these three groups that responded strongly to CS-shock. We also identified two clusters which responded primarily to CS-reward, one which showed excited responses to CS-reward (Cluster 4) and another which was inhibited by CS-reward (Cluster 5). *Drd1a*+ paired group neurons were the largest portion of these two clusters, though neurons from several other groups were present as well. Finally, many neurons from the unpaired group mice, as well as some *Drd1a*+ and *Drd2*+ neurons from paired group mice, were not strongly responsive to either CS (Cluster 6). Altogether, these data showed that *Drd2*+ neurons were primarily responsible for mediating responses to conditioned cues of negative valence in the ASt. The *Drd2*+ neurons also exhibited rapid onset and sustained responses, consistent with the requirements for directing defensive responses across behavioral timescales.

Drd2+ ASt neurons are necessary for the expression of conditioned fear

Our calcium imaging data showed that *Drd2*+ ASt neurons robustly encoded conditioned stimuli of negative valence during tone discrimination, which raised the possibility that the activity of these neurons was in fact necessary to direct the expression of conditioned behavioral responses to these stimuli. To investigate this, we examined the effects of reversible optogenetic inhibition of *Drd2*+ ASt neurons in a variation of the two-tone discrimination task used in recording experiments (**Figure 6A**). *Drd2*+ ASt neurons were bilaterally targeted with a viral construct to conditionally express the inhibitory opsin halorhodopsin (NpHR) in *Drd2-Cre* mice (**Figure 6B, S8A**). These mice were first trained to distinguish tones predicting shock and reward delivery, and then, on a subset of trials, 593 nm light was delivered via optic fibers to the ASt, allowing us to assess the within-animal effects of silencing *Drd2*+ ASt neurons on expression of conditioned behaviors. We found that optogenetic inhibition of *Drd2*+ ASt neurons caused a striking reduction in conditioned defensive behaviors (freezing and escape) in response to CS-shock during ‘Laser ON’ trials compared with ‘Laser OFF’ trials (**Figure 6C**). This inhibition of *Drd2*+ ASt neurons had no effect on responses to CS-reward tones presented during the same experimental session, as measured by reward port entry (**Figure 6D**). These behavioral changes were only seen in NpHR group mice, which showed a significant decreased in overall freezing relative to eYFP controls (**Figure 6E**), with no effect on port entry responses to CS-reward observed in either group (**Figure 6F**). Inhibition of *Drd2*+ ASt neurons had no effect on unconditioned freezing behavior in an open field task (**Figure 6G**), indicating that the changes in conditioned behaviors observed in NpHR group mice during the discrimination task were not simply due to overall changes in motor output. We also saw that inhibition of *Drd2*+ ASt neurons was not innately rewarding or aversive, as measured by preference for a ‘laser ON’ area in real-time place preference task (**Figure 6H**), and did not cause any overall change in preference for open arms in an elevated plus maze task, considered a measure of anxiety-related behaviors (**Figure 6I**). We then examined whether the ASt was necessary for conditioned fear responses to an environmental context, rather than to acute sensory cues. To test this, we placed mice in a novel operant chamber and then

instantiated contextual fear conditioning by delivery of unpredicted foot shocks. We returned the mice to this context 24 hours later while also delivering 593 nm light to the ASt. We found that NpHR group mice still showed robust freezing comparable to eYFP controls in the conditioned context despite the inhibition of *Drd2*+ ASt neurons (**Figure 6J**). This indicated that *Drd2*+ ASt neurons were not required for defensive fear responses to a conditioned context, but indeed were specifically required for responses to acute sensory stimuli. This result also further showed that inhibition of *Drd2*+ ASt neurons was not simply driving a motor effect which prevented mice from freezing altogether, but rather was specific to conditioned responses to sensory stimuli. Together, these results demonstrated that the *Drd2*+ ASt neuron population, which our RNA sequencing data showed was a unique feature of the ASt, was in fact critical for defensive behavioral responses to conditioned stimuli of negative valence.

DISCUSSION:

The ASt encodes conditioned stimuli

Here we demonstrate the amygdalostriatal transition zone (ASt) is a genetically distinct brain region from neighboring amygdalar or striatal structures that plays a critical role in encoding stimuli to direct behavioral responses, a previous uncharacterized role for this structure. We find that individual ASt neurons show conditioned responses to cues consistent with encoding valence and behavioral state, including rapid and sustained responses to stimuli of negative valence, which are specifically mediated by the *Drd2+* population within the ASt. Finally, we find that ASt neurons are essential for the expression of conditioned defensive behaviors.

Our findings identify the ASt as a component of the brain circuitry encoding conditioned stimuli. In conceptual models of emotional responses, it has been proposed that sensory information is assigned salience as well as valence, either sequentially or together (Lang, 1995; Schachter and Singer, 1962), which then serves to direct selection of a behavioral response. Within this framework, ASt neurons appear to encode the learned significance of cues of both positive and negative valence, and not simply sensory information or salience of stimuli. This role is supported by our electrophysiological recordings of ASt neurons, which showed robust responses to auditory cues that predicted shocks or rewards but only in paired group mice, and not in unpaired controls which received the same number of cue, shock and reward presentations but in randomized order and explicitly unpaired. Consequently, the responses seen in paired group mice cannot simply be sensory responses to the auditory cue, or even elevated responses due to sensitization or heightened arousal from receiving rewards and punishments, as these would have been present in unpaired controls as well but were not seen (Rescorla, 1967). Furthermore, while the information encoded in the ASt may be necessary to direct behavioral responses, in both paired and unpaired group mice, ASt neuron activity was not directly encoding specific motor outputs on subsecond timescales. Thus, we can attribute the changes in ASt neurons' cue responses to encoding the predictive value of the cues, which is the sole distinction between the groups. We also saw markedly distinct directions of response for neural trajectories of ASt neurons in response to cues predicting shock and reward, which is consistent with these neurons encoding valence rather than salience.

Sustained responses and defensive behaviors are mediated by the ASt

A remarkable feature of ASt neurons that we observed was the sustained nature of responses to stimuli during discrimination tasks. Our recordings showed that the ASt neurons had significantly greater sustained responses to stimuli of negative valence than adjacent regions, including the TS and CeA. In the brain, sustained responses in neurons can be found at both 'lower' and 'higher' level representations of stimuli. Regions which represent raw sensory information, such as the sensory thalamus, have been shown to track features of stimuli throughout their duration with sustained responses (Bartlett, 2013; Leppla et al., 2022). However, sustained responses are also seen in the prefrontal cortex (PFC), where in both primates and humans they appears to serve as a high-level neural correlate for representation of task features in working memory (Curtis and Sprague, 2021). Indeed, rodents trained in similar behavioral paradigms to those in the present study have shown sustained responses to conditioned stimuli in PFC neurons but comparatively transient responses in the amygdala (Burgos-Robles et al., 2017, 2009). The ASt appears unique in that it is integrated with amygdalar circuits known to mediate valence processing within the limbic system and responds rapidly to stimuli, but shows longer time-scale responses with sustained activity tracking the full duration of stimuli and not simply the stimulus onset as seen in the amygdala (Goosens and Maren, 2004; Li et al., 2022; Quirk et al., 1995; Whittle et al., 2021). What is the purpose of this combination of features in the ASt? We propose that encoding of sustained valence would be of value to orchestrate rapid and continuous behavioral responses to stimuli when it is necessary. Transient responses to stimuli are suitable for cases such as reward

or pursuit behaviors initiated by an animal, or to trigger aspects of emotional responses such as endocrine and stress hormone responses (Ulrich-Lai and Herman, 2009). In the case of defensive responses to threats, however, a neural correlate tracking the full duration of an aversive stimuli would be ideally suited to continuously maintain a behavioral state critical for survival.

Consistent with this proposed role, we found that activity of ASt neurons is indeed crucial for defensive behaviors across behaviorally-relevant timescales. Inhibition of *Drd2*+ ASt neurons, the largest population in the region, caused a striking reduction in freezing behaviors in response to a shock-predicting cue while leaving reward responses unaffected. Importantly, we believe our findings complement rather than contradict the large body of work examining amygdalar circuits mediating learned associations. Many studies have shown that the amygdala complex, especially outputs from the CeA to the periaqueductal grey (PAG), are essential for expression of conditioned fear (Fadok et al., 2017; Keifer et al., 2015; LeDoux et al., 1988; Tovote et al., 2016). Indeed, while inhibition of the ASt did markedly reduce defensive behaviors, there was still considerable residual defensive behaviors in response to the cue (~50% of normal levels), consistent with the fact that the entire 'canonical' amygdala pathway was fully intact as our manipulations targeted only the ASt.

Thus, it seems likely that the output of *Drd2*+ ASt neurons acts in concert with these canonical amygdala circuits and drives defensive behaviors directed via the basal ganglia in a complementary manner to targets of CeA output. It is likely that the ASt and CeA have functional redundancy in some cases but may also have specialized roles for different aspects of fear response and defensive behaviors. For instance, one noteworthy finding in our study was that inhibiting *Drd2*+ ASt neurons had no effect on contextual freezing responses, despite the same manipulation dramatically reducing freezing to auditory cues. The BLA and CeA have been shown to be critical for contextual fear conditioning (Goosens and Maren, 2001) and the hippocampus, a critical structure for spatial and contextual learning (Danielson et al., 2016), sends robust projections to the BLA but not the ASt (Kim and Cho, 2020, 2017). Thus, the ASt may not receive necessary spatial information and play little or no role in contextual freezing, which is instead almost entirely mediated by pathways involving the BLA and CeA. The ASt therefore appears to be critical for sustained behavioral responses to acute sensory stimuli, but not required for responses to environmental context. Further study will be needed to delineate in greater detail the specific conditions and motivated behaviors where the ASt plays an important role. However, our identification of a novel role for the ASt in expression of conditioned behaviors raises some important technical considerations for future studies of amygdala function. Off-target effects on the ASt have never been considered as a potential confound for studies of other amygdalar nuclei, and the ASt is located directly in the vertical path of stereotaxic manipulations targeting the BLA or CeA. Thus, viral injections or pharmacological compounds targeting these nuclei could also inadvertently affect the ASt, which could drive behavioral and cognitive effects that confound interpretation of experimental results. We believe that careful control of manipulations targeting the ASt and amygdalar nuclei will be necessary to clearly distinguish the shared and distinct functions of these two regions.

The ASt in models of valence encoding

How does the ASt fit in the hierarchy of established circuit models for encoding valence to direct behavior? With respect to the amygdala complex, two major models are possible. First, the ASt may be downstream of the amygdala complex, relying on input from the lateral amygdala for ASt neuron responses to conditioned stimuli, and functioning as an output nucleus of the amygdala complex like the CeA. Second, the ASt may act as a parallel pathway to amygdala, capable of encoding conditioned stimuli and directing behavioral responses independently of the amygdala complex. The first model is supported by the robust and rapid projection from the LA to the ASt, which is a key anatomical feature that distinguishes it from the rest of the striatum (Jolkkonen et al., 2001; Wang et al., 2002). The LA is known to be a site where synapses are potentiated to encode fear memory (Blair et al., 2001), and so it is possible that responses to conditioned

stimuli in the ASt to direct behavior are dependent on input from the LA. In contrast, it is also possible the ASt acts independently; synapses from thalamic or cortical projections to the ASt could be directly potentiated to encode learned associations, allowing the ASt to respond to stimuli independently from input from the amygdala. In addition to these two major models, it is also possible that amygdalar inputs to the ASt play an important role in learning, but not expression, of conditioned responses. Determining the functional role of the LA projection to the ASt and investigating plasticity at ASt synapses will be critical areas for future investigation to understand the relationship of the ASt to the amygdala complex. Interestingly, the ASt, along with the tail of striatum, receives a unique dopaminergic projection which carries information pertaining to novelty and external threat, rather than recording reward prediction error like the dopaminergic signal from medial DA neurons (Menegas et al., 2018) Determining the role of this dopaminergic signal in modulating the activity of ASt neurons will likely be critical for understanding the acquisition of conditioned responses and the overall function of the ASt.

The ASt is uniquely situated to complement known basal ganglia circuits mediating defensive action selection and execution, serving as a distinct subregion of the striatum with a unique functional specialization. The transition from action to habits (Robbins and Everitt, 2002) has been proposed to be mediated through cortico-striatal loops in the basal ganglia (Haber, 2016; Heilbronner et al., 2018)(Haber), and we speculate that the ASt could serve as a shortcut to directly connect the circuits important for evaluation of stimuli directly to those for motor execution. Previous studies of striatal pathways have shown that *Drd1a*+ 'direct pathway' MSNs and *Drd2*+ 'indirect pathway' have divergent roles in controlling reinforcement and aversive learning (Cox and Witten, 2019; Kravitz et al., 2012; Nakanishi et al., 2014, 2014). *Drd2*+ neurons are broadly thought to be important for responses to aversive stimuli (Nakanishi et al., 2014), though studies of striatal circuits have overwhelmingly focused on reward learning paradigms rather than fear learning as in the amygdala. Our data suggests a specialized role for the ASt in responding to stimuli of negative valence; while subsets of ASt neurons did respond to positive and negative stimuli, the ASt was highly enriched for *Drd2*+ neurons that responded specifically to stimuli of negative valence, and inhibition of these neurons only affected conditioned responses to aversive stimuli and not reward responses. This is compatible with proposed models of the striatal indirect pathway as a key circuit for motor output elicited by aversive stimuli, suggesting that the sustained activity in the ASt may act to suppress competing actions to facilitate the selection and execution of defensive behaviors. Regardless of whether the ASt is viewed in the context of amygdala or striatal circuits, it does appear to serve as a specialized structure for mediating defensive responses to aversive stimuli. This role for the ASt would also be consistent with a 'divergent paths' model of valence processing (Tye, 2018), where different sensory inputs mediating CS information can be potentiated on distinct efferent circuits in order to mediate appropriate responses to stimuli of positive and negative valence.

ASt neurons have distinct genetic identities

In addition to our functional dissection of ASt neuron activity in motivated behaviors, we also examined the cell type composition and transcriptomic profile of the ASt. The most notable features of the ASt were the greater proportion of *Drd2*+ MSNs compared to *Drd1a*+ MSNs, a unique feature relative to other regions of the striatum, and that ASt neurons were identifiable as genetically distinct subclusters within those MSN types relative to adjacent GABAergic structures the tail of striatum, dorsal striatum, and central nucleus of the amygdala. We found these differences in clustering were due to the unique expression of genes in the ASt relative to these other target regions, with hundreds of differentially expressed genes (DEGs) in *Drd1a*+ and *Drd2*+ ASt neurons. Intriguingly, these DEGs included several synaptic adhesion molecules such as cadherin 6 and integrin 6, which, in addition to serving as marker genes enriched in the ASt, are likely candidates responsible for establishing the unique connectivity of the ASt. The ASt receives robust projections from thalamic and cortical structures (Barsy et al., 2020; Doron and Ledoux, 1999; Hunnicutt et al., 2016; LeDoux et al., 1990; McDonald, 1998; Shi and Cassell, 1999, 1998, 1997), as well as from the lateral amygdala

(Jolkkonen et al., 2001; Wang et al., 2002), and the formation of this circuit connectivity is likely directed by the expression of genes such as such as adhesion molecules and axon guidance factors. The variation in gene expression between regions was much higher in some cell types than others; while *Drd1a* and *Drd2*-expressing MSNs showed considerable variability in gene expression, non-neuronal cells such as astrocytes, microglia and oligodendrocytes showed far fewer DEGs between regions. In the striatum there is considerable range of inputs and outputs that vary with topography, including the cortical regions which project to each subregion of striatum (Graybiel, 1983; Haber, 2016; Hunnicutt et al., 2016). The changes in expression of genes in MSNs that we observed throughout different subregions could be an underlying molecular basis for establishing these broad patterns of connectivity.

Conclusion

Our findings provide the first evidence that the ASt is an important region for encoding responses to emotionally significant stimuli, a previously unknown role for this structure. Consequently, the present study also identifies the ASt as a novel site of interest in neurological disorders where normal responses to stimuli are disrupted. Valence assignment and responses to stimuli are disrupted in depression, anxiety, and post-traumatic stress disorder (Disner et al., 2011; Kaviani et al., 2004; Morey et al., 2015; Ray et al., 2009). The amygdala complex has been widely studied as a key site for these disorders (Davis, 1992), but the possible contribution of the ASt has never been investigated. Since ASt neurons have distinct genetic identities and downstream targets than the rest of the amygdala complex, these circuits could represent vital new targets for the design of therapeutic approaches for these disorders.

REFERENCES:

Allsop, S.A., Wichmann, R., Mills, F., Burgos-Robles, A., Chang, C.-J., Felix-Ortiz, A.C., Vienne, A., Beyeler, A., Izadmehr, E.M., Glober, G., Cum, M.I., Stergiadou, J., Anandalingam, K.K., Farris, K., Namburi, P., Leppla, C.A., Weddington, J.C., Nieh, E.H., Smith, A.C., Ba, D., Brown, E.N., Tye, K.M., 2018. Corticoamygdala Transfer of Socially Derived Information Gates Observational Learning. Cell 173, 1329-1342.e18. https://doi.org/10.1016/j.cell.2018.04.004

Balleine, B.W., O'Doherty, J.P., 2010. Human and Rodent Homologies in Action Control: Corticostriatal Determinants of Goal-Directed and Habitual Action. Neuropsychopharmacol 35, 48–69. https://doi.org/10.1038/npp.2009.131

Barsy, B., Kocsis, K., Magyar, A., Babiczky, Á., Szabó, M., Veres, J.M., Hillier, D., Ulbert, I., Yizhar, O., Mátyás, F., 2020. Associative and plastic thalamic signaling to the lateral amygdala controls fear behavior. Nat Neurosci 23, 625–637. https://doi.org/10.1038/s41593-020-0620-z

Bartlett, E.L., 2013. The organization and physiology of the auditory thalamus and its role in processing acoustic features important for speech perception. Brain Lang 126, 29–48. https://doi.org/10.1016/j.bandl.2013.03.003

Blair, H.T., Schafe, G.E., Bauer, E.P., Rodrigues, S.M., LeDoux, J.E., 2001. Synaptic Plasticity in the Lateral Amygdala: A Cellular Hypothesis of Fear Conditioning. Learn. Mem. 8, 229–242. https://doi.org/10.1101/lm.30901

Bordi, F., LeDoux, J., Clugnet, M.C., Pavlides, C., 1993. Single-unit activity in the lateral nucleus of the amygdala and overlying areas of the striatum in freely behaving rats: rates, discharge patterns, and responses to acoustic stimuli. Behav Neurosci 107, 757–769. https://doi.org/10.1037/0735-7044.107.5.757

Burgos-Robles, A., Kimchi, E.Y., Izadmehr, E.M., Porzenheim, M.J., Ramos-Guasp, W.A., Nieh, E.H., Felix-Ortiz, A.C., Namburi, P., Leppla, C.A., Presbrey, K.N., Anandalingam, K.K., Pagan-Rivera, P.A., Anahtar, M., Beyeler, A., Tye, K.M., 2017. Amygdala inputs to prefrontal cortex guide behavior amid conflicting cues of reward and punishment. Nat Neurosci 20, 824–835. https://doi.org/10.1038/nn.4553

Burgos-Robles, A., Vidal-Gonzalez, I., Quirk, G.J., 2009. Sustained conditioned responses in prelimbic prefrontal neurons are correlated with fear expression and extinction failure. J Neurosci 29, 8474–8482. https://doi.org/10.1523/JNEUROSCI.0378-09.2009

Ciocchi, S., Herry, C., Grenier, F., Wolff, S.B.E., Letzkus, J.J., Vlachos, I., Ehrlich, I., Sprengel, R., Deisseroth, K., Stadler, M.B., Muller, C., Luthi, A., 2010. Encoding of conditioned fear in central amygdala inhibitory circuits. Nature 468, 277–282. https://doi.org/10.1038/nature09559

Cox, J., Witten, I.B., 2019. Striatal circuits for reward learning and decision-making. Nat Rev Neurosci 20, 482–494. https://doi.org/10.1038/s41583-019-0189-2

Cui, G., Jun, S.B., Jin, X., Pham, M.D., Vogel, S.S., Lovinger, D.M., Costa, R.M., 2013. Concurrent activation of striatal direct and indirect pathways during action initiation. Nature 494, 238–242. https://doi.org/10.1038/nature11846

Cunningham, J.P., Yu, B.M., 2014. Dimensionality reduction for large-scale neural recordings. Nat Neurosci 17, 1500–1509. https://doi.org/10.1038/nn.3776

Curtis, C.E., Sprague, T.C., 2021. Persistent Activity During Working Memory From Front to Back. Frontiers in Neural Circuits 15.

Danielson, N.B., Kaifosh, P., Zaremba, J.D., Lovett-Barron, M., Tsai, J., Denny, C.A., Balough, E.M., Goldberg, A.R., Drew, L.J., Hen, R., Losonczy, A., Kheirbek, M.A., 2016. Distinct Contribution of Adult-Born Hippocampal Granule Cells to Context Encoding. Neuron 90, 101–112. https://doi.org/10.1016/j.neuron.2016.02.019

Davis, M., 1992. The role of the amygdala in fear and anxiety. Annu. Rev. Neurosci. 15, 353–375. https://doi.org/10.1146/annurev.ne.15.030192.002033

Disner, S.G., Beevers, C.G., Haigh, E.A.P., Beck, A.T., 2011. Neural mechanisms of the cognitive model of depression. Nature Reviews Neuroscience 12, 467–477. https://doi.org/10.1038/nrn3027

Doron, N.N., Ledoux, J.E., 1999. Organization of projections to the lateral amygdala from auditory and visual areas of the thalamus in the rat. Journal of Comparative Neurology 412, 383–409. https://doi.org/10.1002/(SICI)1096-9861(19990927)412:3<383::AID-CNE2>3.0.CO;2-5

Fadok, J.P., Krabbe, S., Markovic, M., Courtin, J., Xu, C., Massi, L., Botta, P., Bylund, K., Müller, C., Kovacevic, A., Tovote, P., Lüthi, A., 2017. A competitive inhibitory circuit for selection of active and passive fear responses. Nature 542, 96–100. https://doi.org/10.1038/nature21047

Fanselow, M.S., LeDoux, J.E., 1999. Why we think plasticity underlying Pavlovian fear conditioning occurs in the basolateral amygdala. Neuron 23, 229–232. https://doi.org/10.1016/s0896-6273(00)80775-8

Gagnon, D., Petryszyn, S., Sanchez, M.G., Bories, C., Beaulieu, J.M., De Koninck, Y., Parent, A., Parent, M., 2017. Striatal Neurons Expressing D1 and D2 Receptors are Morphologically Distinct and Differently Affected by Dopamine Denervation in Mice. Sci Rep 7, 41432. https://doi.org/10.1038/srep41432

Gallagher, M., Holland, P.C., 1994. The amygdala complex: multiple roles in associative learning and attention. Proceedings of the National Academy of Sciences 91, 11771–11776. https://doi.org/10.1073/pnas.91.25.11771

Gangarossa, G., Espallergues, J., Mailly, P., De Bundel, D., De Kerchove D'Exaerde, A., Hervé, D., Girault, J.-A., Valjent, E., Krieger, P., 2013. Spatial distribution of D1R- and D2R-expressing medium-sized spiny neurons differs along the rostro-caudal axis of the mouse dorsal striatum. Frontiers in Neural Circuits 7. https://doi.org/10.3389/fncir.2013.00124

Gerfen, C.R., Engber, T.M., Mahan, L.C., Susel, Z., Chase, T.N., Monsma, F.J., Sibley, D.R., 1990. D1 and D2 dopamine receptor-regulated gene expression of striatonigral and striatopallidal neurons. Science 250, 1429–1432.

Gerfen, C.R., Surmeier, D.J., 2011. Modulation of striatal projection systems by dopamine. Annu Rev Neurosci 34, 441–466. https://doi.org/10.1146/annurev-neuro-061010-113641

Glaser, J.I., Benjamin, A.S., Chowdhury, R.H., Perich, M.G., Miller, L.E., Kording, K.P., 2020. Machine Learning for Neural Decoding. eNeuro 7. https://doi.org/10.1523/ENEURO.0506-19.2020

Gong, S., Doughty, M., Harbaugh, C.R., Cummins, A., Hatten, M.E., Heintz, N., Gerfen, C.R., 2007. Targeting Cre recombinase to specific neuron populations with bacterial artificial chromosome constructs. J. Neurosci. 27, 9817–9823. https://doi.org/10.1523/JNEUROSCI.2707-07.2007

Goosens, K.A., Maren, S., 2004. NMDA receptors are essential for the acquisition, but not expression, of conditional fear and associative spike firing in the lateral amygdala. European Journal of Neuroscience 20, 537–548. https://doi.org/10.1111/j.1460-9568.2004.03513.x

Goosens, K.A., Maren, S., 2001. Contextual and Auditory Fear Conditioning are Mediated by the Lateral, Basal, and Central Amygdaloid Nuclei in Rats. Learn Mem 8, 148–155. https://doi.org/10.1101/lm.37601

Graybiel, A.M., 1983. Compartmental Organization of the Mammalian Striatum, in: Changeux, J.-P., Glowinski, J., Imbert, M., Bloom, F.E. (Eds.), Progress in Brain Research. Elsevier, pp. 247–256. https://doi.org/10.1016/S0079-6123(08)60026-6

Haber, S.N., 2016. Corticostriatal circuitry. Dialogues in Clinical Neuroscience 18, 7–21. https://doi.org/10.31887/DCNS.2016.18.1/shaber

Haubensak, W., Kunwar, P.S., Cai, H., Ciocchi, S., Wall, N.R., Ponnusamy, R., Biag, J., Dong, H.-W., Deisseroth, K., Callaway, E.M., Fanselow, M.S., Luthi, A., Anderson, D.J., 2010. Genetic dissection of an amygdala microcircuit that gates conditioned fear. Nature 468, 270–276. https://doi.org/10.1038/nature09553

Heilbronner, S.R., Meyer, M.A.A., Choi, E.Y., Haber, S.N., 2018. How do cortico-striatal projections impact on downstream pallidal circuitry? Brain Struct Funct 223, 2809–2821. https://doi.org/10.1007/s00429-018-1662-9

Hicks, S.C., Townes, F.W., Teng, M., Irizarry, R.A., 2018. Missing data and technical variability in single-cell RNA-sequencing experiments. Biostatistics 19, 562–578. https://doi.org/10.1093/biostatistics/kxx053

Hunnicutt, B.J., Jongbloets, B.C., Birdsong, W.T., Gertz, K.J., Zhong, H., Mao, T., 2016. A comprehensive excitatory input map of the striatum reveals novel functional organization. eLife 5, e19103. https://doi.org/10.7554/eLife.19103

Jennings, J.H., Sparta, D.R., Stamatakis, A.M., Ung, R.L., Pleil, K.E., Kash, T.L., Stuber, G.D., 2013. Distinct extended amygdala circuits for divergent motivational states. Nature 496, 224–8. https://doi.org/10.1038/nature12041

Johansen, J.P., Hamanaka, H., Monfils, M.H., Behnia, R., Deisseroth, K., Blair, H.T., LeDoux, J.E., 2010. Optical activation of lateral amygdala pyramidal cells instructs associative fear learning. Proceedings of the National Academy of Sciences 107, 12692–12697. https://doi.org/10.1073/pnas.1002418107

Jolkkonen, E., Pikkarainen, M., Kemppainen, S., Pitkänen, A., 2001. Interconnectivity between the amygdaloid complex and the amygdalostriatal transition area: a PHA-L study in rat. J. Comp. Neurol. 431, 39–58.

Josselyn, S.A., Köhler, S., Frankland, P.W., 2015. Finding the engram. Nat Rev Neurosci 16, 521–534. https://doi.org/10.1038/nrn4000

Kaviani, H., Gray, J.A., Checkley, S.A., Raven, P.W., Wilson, G.D., Kumari, V., 2004. Affective modulation of the startle response in depression: influence of the severity of depression, anhedonia, and anxiety. Journal of Affective Disorders 83, 21–31. https://doi.org/10.1016/j.jad.2004.04.007

Keifer, O.P., Hurt, R.C., Ressler, K.J., Marvar, P.J., 2015. The Physiology of Fear: Reconceptualizing the Role of the Central Amygdala in Fear Learning. Physiology 30, 389–401. https://doi.org/10.1152/physiol.00058.2014

Kim, J., Pignatelli, M., Xu, S., Itohara, S., Tonegawa, S., 2016. Antagonistic negative and positive neurons of the basolateral amygdala. Nat Neurosci 19, 1636–1646. https://doi.org/10.1038/nn.4414

Kim, W.B., Cho, J.-H., 2020. Encoding of contextual fear memory in hippocampal–amygdala circuit. Nat Commun 11, 1382. https://doi.org/10.1038/s41467-020-15121-2

Kim, W.B., Cho, J.-H., 2017. Synaptic Targeting of Double-Projecting Ventral CA1 Hippocampal Neurons to the Medial Prefrontal Cortex and Basal Amygdala. J Neurosci 37, 4868–4882. https://doi.org/10.1523/JNEUROSCI.3579-16.2017

Kong, M.-S., Zweifel, L.S., 2021. Central amygdala circuits in valence and salience processing. Behavioural Brain Research 410, 113355. https://doi.org/10.1016/j.bbr.2021.113355

Kravitz, A.V., Freeze, B.S., Parker, P.R.L., Kay, K., Thwin, M.T., Deisseroth, K., Kreitzer, A.C., 2010. Regulation of parkinsonian motor behaviors by optogenetic control of basal ganglia circuitry. Nature 466, 622–626. https://doi.org/10.1038/nature09159

Kravitz, A.V., Tye, L.D., Kreitzer, A.C., 2012. Distinct roles for direct and indirect pathway striatal neurons in reinforcement. Nat. Neurosci. 15, 816–818. https://doi.org/10.1038/nn.3100

Lang, P.J., 1995. The emotion probe. Studies of motivation and attention. Am Psychol 50, 372–385. https://doi.org/10.1037//0003-066x.50.5.372

LeDoux, J.E., 1992. Brain mechanisms of emotion and emotional learning. Current Opinion in Neurobiology 2, 191–197. https://doi.org/10.1016/0959-4388(92)90011-9

LeDoux, J.E., Farb, C., Ruggiero, D.A., 1990. Topographic organization of neurons in the acoustic thalamus that project to the amygdala. J. Neurosci. 10, 1043–1054. https://doi.org/10.1523/JNEUROSCI.10-04-01043.1990

LeDoux, J.E., Iwata, J., Cicchetti, P., Reis, D.J., 1988. Different projections of the central amygdaloid nucleus mediate autonomic and behavioral correlates of conditioned fear. J. Neurosci. 8, 2517–2529. https://doi.org/10.1523/JNEUROSCI.08-07-02517.1988

Leppla, C.A., Keyes, L.R., Glober, G., Matthews, G.A., Batra, K., Jay, M., Feng, Y., Chen, H.S., Mills, F., Delahanty, J., Olsen, J., Nieh, E.H., Namburi, P., Wildes, C., Wichmann, R., Beyeler, A., Kimchi, E.Y., Tye, K.M., 2022. Thalamus sends information about arousal but not valence to the amygdala. https://doi.org/10.1101/2022.07.18.500471

Li, H., Namburi, P., Olson, J.M., Borio, M., Lemieux, M.E., Beyeler, A., Calhoon, G.G., Hitora-Imamura, N., Coley, A.A., Libster, A., Bal, A., Jin, X., Wang, H., Jia, C., Choudhury, S.R., Shi, X., Felix-Ortiz, A.C., de la Fuente, V., Barth, V.P., King, H.O., Izadmehr, E.M., Revanna, J.S., Batra, K., Fischer, K.B., Keyes, L.R., Padilla-Coreano, N., Siciliano, C.A., McCullough, K.M., Wichmann, R., Ressler, K.J., Fiete, I.R., Zhang, F., Li, Y., Tye, K.M., 2022. Neurotensin orchestrates valence assignment in the amygdala. Nature. https://doi.org/10.1038/s41586-022-04964-y

Lobo, M.K., Covington, H.E., Chaudhury, D., Friedman, A.K., Sun, H., Damez-Werno, D., Dietz, D.M., Zaman, S., Koo, J.W., Kennedy, P.J., Mouzon, E., Mogri, M., Neve, R.L., Deisseroth, K., Han, M.-H., Nestler, E.J., 2010. Cell Type-Specific Loss of BDNF Signaling Mimics Optogenetic Control of Cocaine Reward. Science 330, 385–390. https://doi.org/10.1126/science.1188472

Marcinkiewcz, C.A., Mazzone, C.M., D'Agostino, G., Halladay, L.R., Hardaway, J.A., DiBerto, J.F., Navarro, M., Burnham, N., Cristiano, C., Dorrier, C.E., Tipton, G.J., Ramakrishnan, C., Kozicz, T., Deisseroth, K., Thiele, T.E., McElligott, Z.A., Holmes, A., Heisler, L.K., Kash, T.L., 2016. Serotonin engages an anxiety and fear-promoting circuit in the extended amygdala. Nature 537, 97–101. https://doi.org/10.1038/nature19318

Maren, S., 2005. Synaptic Mechanisms of Associative Memory in the Amygdala. Neuron 47, 783–786. https://doi.org/10.1016/j.neuron.2005.08.009

Maren, S., Quirk, G.J., 2004. Neuronal signalling of fear memory. Nat. Rev. Neurosci. 5, 844–852. https://doi.org/10.1038/nrn1535

Markowitz, J.E., Gillis, W.F., Beron, C.C., Neufeld, S.Q., Robertson, K., Bhagat, N.D., Peterson, R.E., Peterson, E., Hyun, M., Linderman, S.W., Sabatini, B.L., Datta, S.R., 2018. The Striatum Organizes 3D Behavior via Moment-to-Moment Action Selection. Cell 174, 44-58.e17. https://doi.org/10.1016/j.cell.2018.04.019

Märtin, A., Calvigioni, D., Tzortzi, O., Fuzik, J., Wärnberg, E., Meletis, K., 2019. A Spatiomolecular Map of the Striatum. Cell Rep 29, 4320-4333.e5. https://doi.org/10.1016/j.celrep.2019.11.096

McDonald, A.J., 1998. Cortical pathways to the mammalian amygdala. Progress in Neurobiology 55, 257–332. https://doi.org/10.1016/S0301-0082(98)00003-3

Menegas, W., Akiti, K., Amo, R., Uchida, N., Watabe-Uchida, M., 2018. Dopamine neurons projecting to the posterior striatum reinforce avoidance of threatening stimuli. Nat Neurosci 21, 1421–1430. https://doi.org/10.1038/s41593-018-0222-1

Miyamoto, Y., Katayama, S., Shigematsu, N., Nishi, A., Fukuda, T., 2018. Striosome-based map of the mouse striatum that is conformable to both cortical afferent topography and uneven distributions of dopamine D1 and D2 receptor-expressing cells. Brain Struct Funct 223, 4275–4291. https://doi.org/10.1007/s00429-018-1749-3

Miyamoto, Y., Nagayoshi, I., Nishi, A., Fukuda, T., 2019. Three divisions of the mouse caudal striatum differ in the proportions of dopamine D1 and D2 receptor-expressing cells, distribution of dopaminergic axons, and composition of cholinergic and GABAergic interneurons. Brain Struct Funct 224, 2703–2716. https://doi.org/10.1007/s00429-019-01928-3

Morey, R.A., Dunsmoor, J.E., Haswell, C.C., Brown, V.M., Vora, A., Weiner, J., Stjepanovic, D., Wagner, H.R., LaBar, K.S., 2015. Fear learning circuitry is biased toward generalization of fear associations in posttraumatic stress disorder. Transl Psychiatry 5, e700. https://doi.org/10.1038/tp.2015.196

Nakanishi, S., Hikida, T., Yawata, S., 2014. Distinct dopaminergic control of the direct and indirect pathways in reward-based and avoidance learning behaviors. Neuroscience, The Ventral Tegmentum and Dopamine: A New Wave of Diversity 282, 49–59. https://doi.org/10.1016/j.neuroscience.2014.04.026

Nelson, A.B., Kreitzer, A.C., 2014. Reassessing models of basal ganglia function and dysfunction. Annu Rev Neurosci 37, 117–135. https://doi.org/10.1146/annurev-neuro-071013-013916

Padilla-Coreano, N., Batra, K., Patarino, M., Chen, Z., Rock, R.R., Zhang, R., Hausmann, S.B., Weddington, J.C., Patel, R., Zhang, Y.E., Fang, H.-S., Mishra, S., LeDuke, D.O., Revanna, J., Li, H., Borio, M., Pamintuan, R., Bal, A., Keyes, L.R., Libster, A., Wichmann, R., Mills, F., Taschbach, F.H., Matthews, G.A., Curley, J.P., Fiete, I.R., Lu, C., Tye, K.M., 2022. Cortical ensembles orchestrate social competition through hypothalamic outputs. Nature 603, 667–671. https://doi.org/10.1038/s41586-022-04507-5

Pereira, T.D., Tabris, N., Matsliah, A., Turner, D.M., Li, J., Ravindranath, S., Papadoyannis, E.S., Normand, E., Deutsch, D.S., Wang, Z.Y., McKenzie-Smith, G.C., Mitelut, C.C., Castro, M.D., D'Uva, J., Kislin, M., Sanes, D.H., Kocher, S.D., Wang, S.S.-H., Falkner, A.L., Shaevitz, J.W., Murthy, M., 2022. SLEAP: A deep learning system for multi-animal pose tracking. Nat Methods 19, 486–495. https://doi.org/10.1038/s41592-022-01426-1

Piantadosi, S.C., Zhou, Z.C., Pizzano, C., Pedersen, C.E., Nguyen, T.K., Thai, S., Stuber, G.D., Bruchas, M.R., 2022. Holographic stimulation of opposing amygdala ensembles bidirectionally modulates valence-specific behavior. https://doi.org/10.1101/2022.07.11.499499

Quirk, G.J., Repa, J.C., LeDoux, J.E., 1995. Fear conditioning enhances short-latency auditory responses of lateral amygdala neurons: Parallel recordings in the freely behaving rat. Neuron 15, 1029–1039. https://doi.org/10.1016/0896-6273(95)90092-6

Ray, W.J., Molnar, C., Aikins, D., Yamasaki, A., Newman, M.G., Castonguay, L., Borkovec, T.D., 2009. Startle response in Generalized Anxiety Disorder. Depression and Anxiety 26, 147–154. https://doi.org/10.1002/da.20479

Redgrave, P., Rodriguez, M., Smith, Y., Rodriguez-Oroz, M.C., Lehericy, S., Bergman, H., Agid, Y., DeLong, M.R., Obeso, J.A., 2010. Goal-directed and habitual control in the basal ganglia: implications for Parkinson's disease. Nat Rev Neurosci 11, 760–772. https://doi.org/10.1038/nrn2915

Ren, K., Guo, B., Dai, C., Yao, H., Sun, T., Liu, X., Bai, Z., Wang, W., Wu, S., 2017. Striatal Distribution and Cytoarchitecture of Dopamine Receptor Subtype 1 and 2: Evidence from Double-Labeling Transgenic Mice. Frontiers in Neural Circuits 11.

Rescorla, R.A., 1967. Pavlovian conditioning and its proper control procedures. Psychol Rev 74, 71–80. https://doi.org/10.1037/h0024109

Robbins, T.W., Everitt, B.J., 2002. Limbic-Striatal Memory Systems and Drug Addiction. Neurobiology of Learning and Memory 78, 625–636. https://doi.org/10.1006/nlme.2002.4103

Romanski, L.M., Clugnet, M.-C., Bordi, F., LeDoux, J.E., 1993. Somatosensory and auditory convergence in the lateral nucleus of the amygdala. Behavioral Neuroscience 107, 444–450. https://doi.org/10.1037/0735-7044.107.3.444

Sah, P., Westbrook, R.F., Lüthi, A., 2008. Fear Conditioning and Long-term Potentiation in the Amygdala. Annals of the New York Academy of Sciences 1129, 88–95. https://doi.org/10.1196/annals.1417.020

Saunders, A., Macosko, E.Z., Wysoker, A., Goldman, M., Krienen, F.M., de Rivera, H., Bien, E., Baum, M., Bortolin, L., Wang, S., Goeva, A., Nemesh, J., Kamitaki, N., Brumbaugh, S., Kulp, D., McCarroll, S.A., 2018. Molecular Diversity and Specializations among the Cells of the Adult Mouse Brain. Cell 174, 1015-1030.e16. https://doi.org/10.1016/j.cell.2018.07.028

Schachter, S., Singer, J.E., 1962. Cognitive, social, and physiological determinants of emotional state. Psychol Rev 69, 379–399. https://doi.org/10.1037/h0046234

Shammah-Lagnado, S.J., Alheid, G.F., Heimer, L., 1999. Afferent connections of the interstitial nucleus of the posterior limb of the anterior commissure and adjacent amygdalostriatal transition area in the rat. Neuroscience 94, 1097–1123. https://doi.org/10.1016/S0306-4522(99)90280-4

Shi, C. -j, Cassell, M.D., 1999. Perirhinal cortex projections to the amygdaloid complex and hippocampal formation in the rat. Journal of Comparative Neurology 406, 299–328. https://doi.org/10.1002/(SICI)1096-9861(19990412)406:3<299::AID-CNE2>3.0.CO;2-9

Shi, C.-J., Cassell, M. d., 1998. Cascade projections from somatosensory cortex to the rat basolateral amygdala via the parietal insular cortex. Journal of Comparative Neurology 399, 469–491. https://doi.org/10.1002/(SICI)1096-9861(19981005)399:4<469::AID-CNE3>3.0.CO;2-#

Shi, C.-J., Cassell, M.D., 1997. Cortical, thalamic, and amygdaloid projections of rat temporal cortex. Journal of Comparative Neurology 382, 153–175. https://doi.org/10.1002/(SICI)1096-9861(19970602)382:2<153::AID-CNE2>3.0.CO;2-2

Stanley, G., Gokce, O., Malenka, R.C., Südhof, T.C., Quake, S.R., 2020. Continuous and Discrete Neuron Types of the Adult Murine Striatum. Neuron 105, 688-699.e8. https://doi.org/10.1016/j.neuron.2019.11.004

Tai, L.H., Lee, A.M., Benavidez, N., Bonci, A., Wilbrecht, L., 2012. Transient stimulation of distinct subpopulations of striatal neurons mimics changes in action value. Nat Neurosci 15, 1281–9. https://doi.org/10.1038/nn.3188

Tovote, P., Esposito, M.S., Botta, P., Chaudun, F., Fadok, J.P., Markovic, M., Wolff, S.B.E., Ramakrishnan, C., Fenno, L., Deisseroth, K., Herry, C., Arber, S., Lüthi, A., 2016. Midbrain circuits for defensive behaviour. Nature 534, 206–212. https://doi.org/10.1038/nature17996

Tye, K.M., 2018. Neural Circuit Motifs in Valence Processing. Neuron 100, 436–452. https://doi.org/10.1016/j.neuron.2018.10.001

Tye, K.M., Prakash, R., Kim, S.Y., Fenno, L.E., Grosenick, L., Zarabi, H., Thompson, K.R., Gradinaru, V., Ramakrishnan, C., Deisseroth, K., 2011. Amygdala circuitry mediating reversible and bidirectional control of anxiety. Nature 471, 358–362.

Tye, K.M., Stuber, G.D., De Ridder, B., Bonci, A., Janak, P.H., 2008. Rapid strengthening of thalamo-amygdala synapses mediates cue–reward learning. Nature 453, 1253–1257.

Ulrich-Lai, Y.M., Herman, J.P., 2009. Neural regulation of endocrine and autonomic stress responses. Nat Rev Neurosci 10, 397–409. https://doi.org/10.1038/nrn2647

Uwano, T., Nishijo, H., Ono, T., Tamura, R., 1995. Neuronal responsiveness to various sensory stimuli, and associative learning in the rat amygdala. Neuroscience 68, 339–361. https://doi.org/10.1016/0306-4522(95)00125-3

Wang, C., Kang-Park, M.-H., Wilson, W.A., Moore, S.D., 2002. Properties of the Pathways From the Lateral Amygdal Nucleus to Basolateral Nucleus and Amygdalostriatal Transition Area. Journal of Neurophysiology 87, 2593–2601. https://doi.org/10.1152/jn.2002.87.5.2593

Weiskrantz, L., 1956. Behavioral changes associated with ablation of the amygdaloid complex in monkeys. Journal of Comparative and Physiological Psychology 49, 381–391. https://doi.org/10.1037/h0088009

Whittle, N., Fadok, J., MacPherson, K.P., Nguyen, R., Botta, P., Wolff, S.B.E., Müller, C., Herry, C., Tovote, P., Holmes, A., Singewald, N., Lüthi, A., Ciocchi, S., 2021. Central amygdala micro-circuits mediate fear extinction. Nat Commun 12, 4156. https://doi.org/10.1038/s41467-021-24068-x

Zheng, G.X.Y., Terry, J.M., Belgrader, P., Ryvkin, P., Bent, Z.W., Wilson, R., Ziraldo, S.B., Wheeler, T.D., McDermott, G.P., Zhu, J., Gregory, M.T., Shuga, J., Montesclaros, L., Underwood, J.G., Masquelier, D.A., Nishimura, S.Y., Schnall-Levin, M., Wyatt, P.W., Hindson, C.M., Bharadwaj, R., Wong, A., Ness, K.D., Beppu, L.W., Deeg, H.J., McFarland, C., Loeb, K.R., Valente, W.J., Ericson, N.G., Stevens, E.A., Radich, J.P., Mikkelsen, T.S., Hindson, B.J., Bielas, J.H., 2017. Massively parallel digital transcriptional profiling of single cells. Nature Communications 8, 14049. https://doi.org/10/f9mbtp

FIGURE LEGENDS:

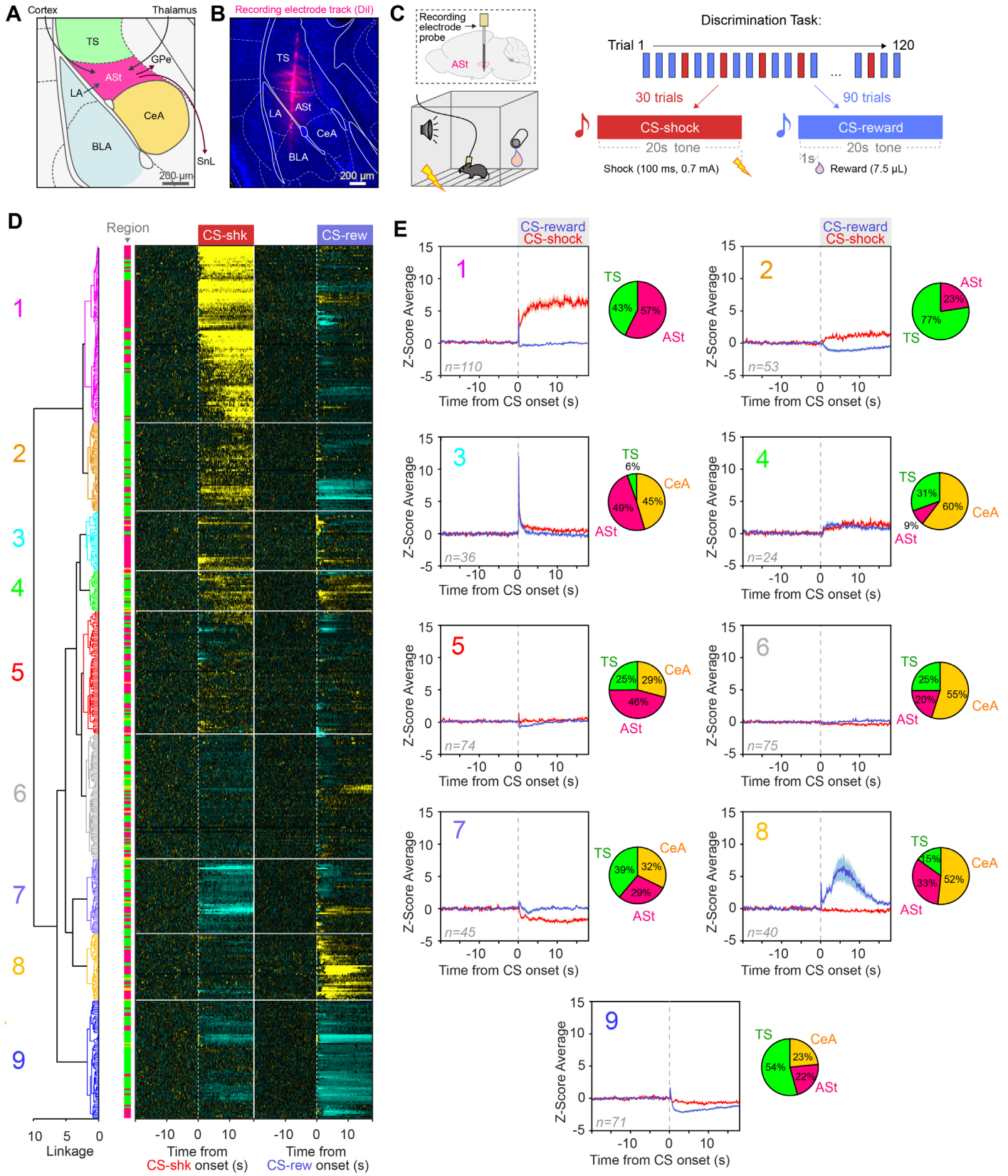

Figure 1

Figure 1. ASt neurons have distinct responses to stimuli of positive and negative valence
(**A**) The amygdalostriatal transition zone (ASt), surrounding regions, and major inputs and outputs of the ASt.
(**B**) Representative image of Neuropixels recording probe targeting the ASt and adjacent regions.
(**C**) Two-tone discrimination task design for *in vivo* electrophysiology recordings.
(**D**) Hierarchical clustering of ASt, tail of striatum (TS) and central nucleus of the amygdala (CeA) neurons based on responses to CS-shock and CS-reward. Dendrogram shows clustering of neurons based on responses to cues of positive and negative valence. Heatmap rows show the mean Z-score PSTH for each individual neuron's responses to both CS-shock and CS-reward in paired group mice (N=15 mice, 222 neurons ASt, 5 mice 280 neurons TS, 2 mice 25 neurons CeA).
(**E**) Z-score average responses to CS-shock and CS-reward in each identified functional cluster. Inset pie charts show the proportion of neurons from each region in that cluster, normalized by number of neurons recorded from each region.

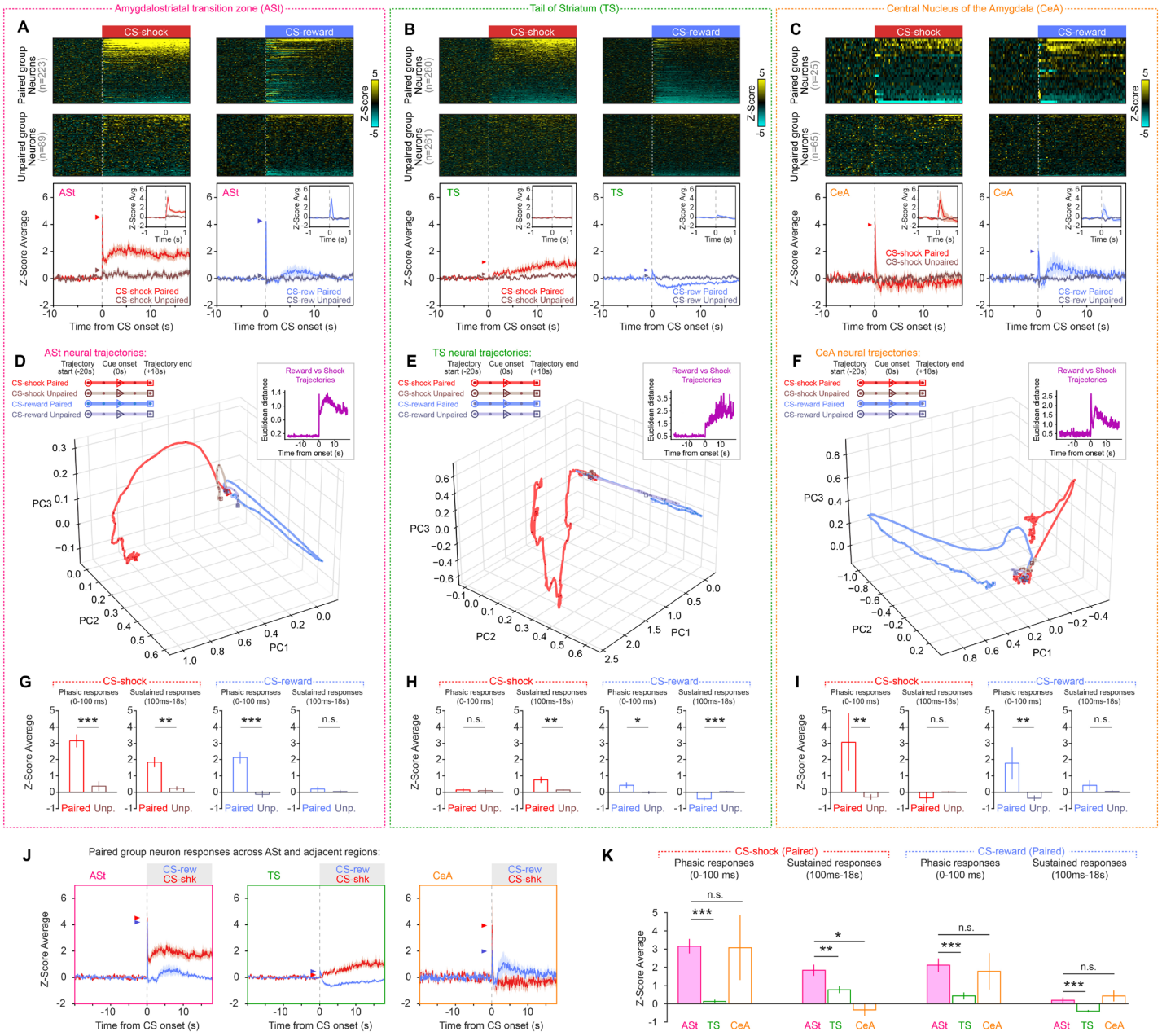

Figure 2

Figure 2. ASt neurons encode sustained conditioned responses to stimuli of negative valence.
(**A-C**) Heat maps and group average of z-score changes in neural firing rate in response to CS-shock and CS-reward in ASt (**A**), TS (**B**), and CeA (**C**). Heatmap rows represent average Z-score PSTH for individual neurons. Arrowheads show average peak z-score during phasic window (0-100 ms). Insets show zoom of mean Z-score at +/-1s at onset of each CS type.
(**D-F**) Neural trajectories of neuron firing rates in ASt (**A**), TS (**B**), and CeA (**C**) in response to conditioned cues of opposing valence. Inset shows that euclidean distance between CS-shock and CS-reward trajectories in paired group mice.
(**G**) ASt neurons show significantly greater phasic responses to CS-shock (Two-tailed t-test, t = 4.228, df = 310, *** p = 0.0000310), sustained responses to CS-shock (Two-tailed t-test, t = 3.232, df = 310, ** p = 0.00136) and phasic responses to CS-reward (Two-tailed t-test, t = 3.810, df = 310, *** p = 0.000167) in paired group mice compared to unpaired controls.
(**H**) TS neurons showed overall little phasic responses to CS-shock (Two-tailed t-test, t = 2.410, df = 539, p = 0.1805), small but significant sustained responses to CS-shock (Two-tailed t-test, t = 3.266, df = 539, ** p = 0.001160), phasic responses to CS-reward (Two-tailed t-test, t = 2.061, df = 539, * p = 0.0398), and sustained inhibitory responses to CS-reward (Two-tailed t-test, t = -5.244, df = 539, *** p = 0.000002251) in paired group mice compared to unpaired controls.
(**I**) CeA neurons showed robust phasic responses to CS-shock (Two-tailed t-test, t = 2.9397, df = 88, ** = p = 0.00419), but no significant sustained responses to CS-shock (Two-tailed t-test, t = -1.529, df = 88, p = 0.129), and phasic responses to CS-reward (Two-tailed t-test, t = 3.127, df = 88, ** p = 0.00239), and a trend towards sustained responses to CS reward (Two-tailed t-test, t = 1.7442, df = 88, p = 0.0846) in paired group mice compared to unpaired controls.
(**J**) Average Z-score responses to CS-shock and CS-reward in paired group mice neurons recorded in tail of striatum (TS), amygdalostriatal transition zone (ASt) and central nucleus of the amygdala.
(**K**) ASt neurons show significantly greater sustained responses to CS-shock than neurons in adjacent TS or CeA regions in paired group mice (One-way ANOVA, * p < 0.05, ** p <0.01, *** p < 0.001, Tukey's multiple comparison test. N=15 mice paired, 4 mice unpaired ASt, 5 mice paired, 4 mice unpaired TS, 2 mice paired, 2 mice unpaired CeA).

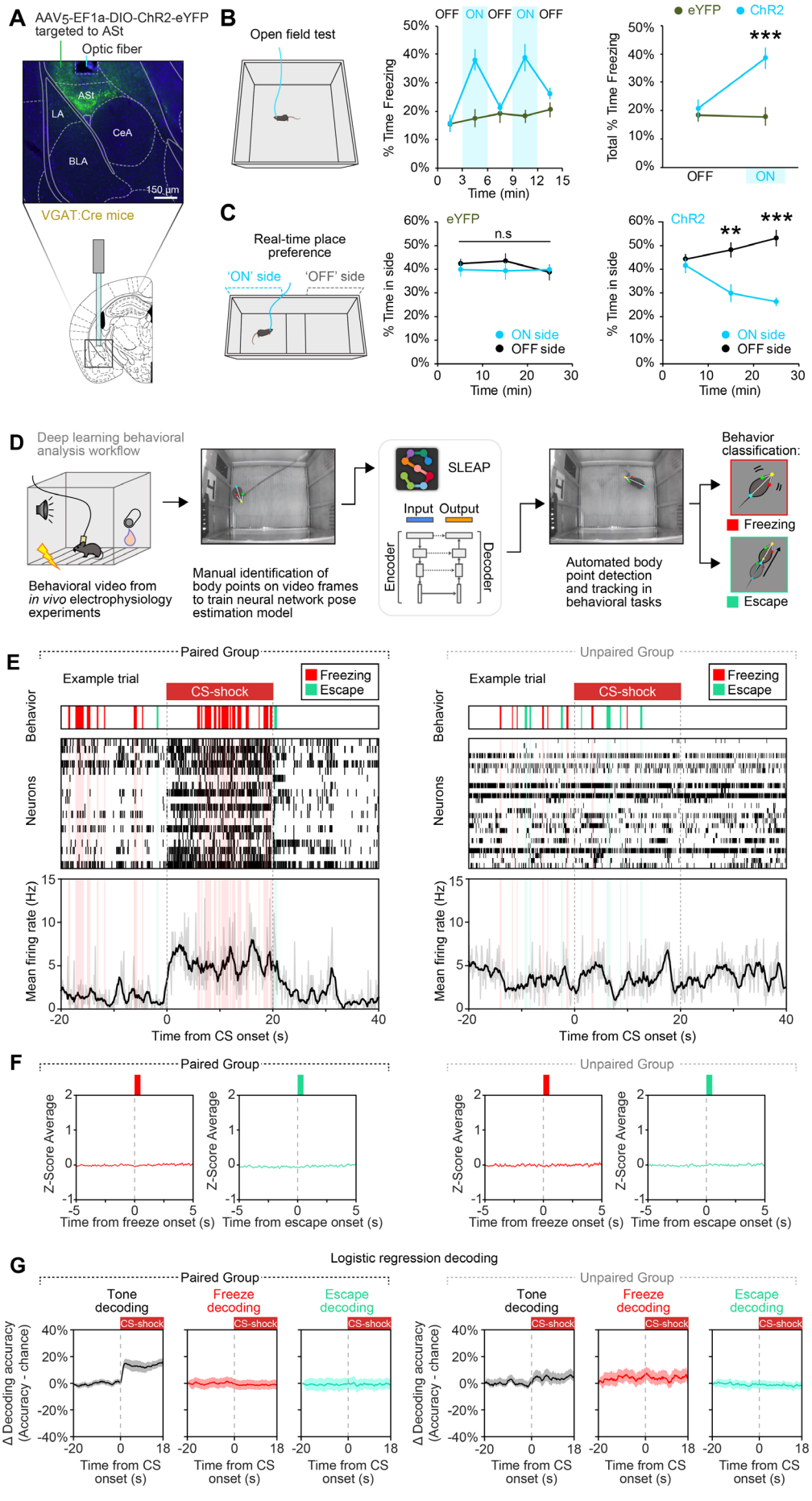

Figure 3

Figure 3. ASt neuron activation drives robust freezing and avoidance behavioral states rather than subsecond motor actions.
(**A**) Targeting strategy and representative image of ChR2 expression in ASt neurons.
(**B**) Optogenetic activation of ASt neurons during light 'ON' epochs of an open field task resulted in a significant increase in freezing in ChR2 group mice (Two-way ANOVA, group x laser interaction $F_{(1,32)} = 10.98$, $p = 0.0023$. Bonferroni post hoc analysis ***$p < 0.001$).
(**C**) ChR2 group mice show increased avoidance of an area paired with optogenetic stimulation in a real-time place preference task (Two-way RM ANOVA, group x laser interaction $F_{(2,42)} = 4.386$, $p = 0.0186$. Bonferroni post hoc analysis ** $p < 0.01$, ***$p < 0.001$). N=8 mice ChR2, 10 mice eYFP.
(**D**) Workflow for classification of defensive behaviors using SLEAP.
(**E**) Representative trials from discrimination task experiments showing simultaneous subsecond behavior, neural spikes, and average neuron firing rate during presentation of CS-shock.
(**F**) Average ASt Z-score responses to onset of freezing and escape behavior motor actions in paired and unpaired group mice.
(**G**) Logistic regression decoder change in performance over time relative to chance level for decoding tone identity, freezing or escape in paired and unpaired group mice.

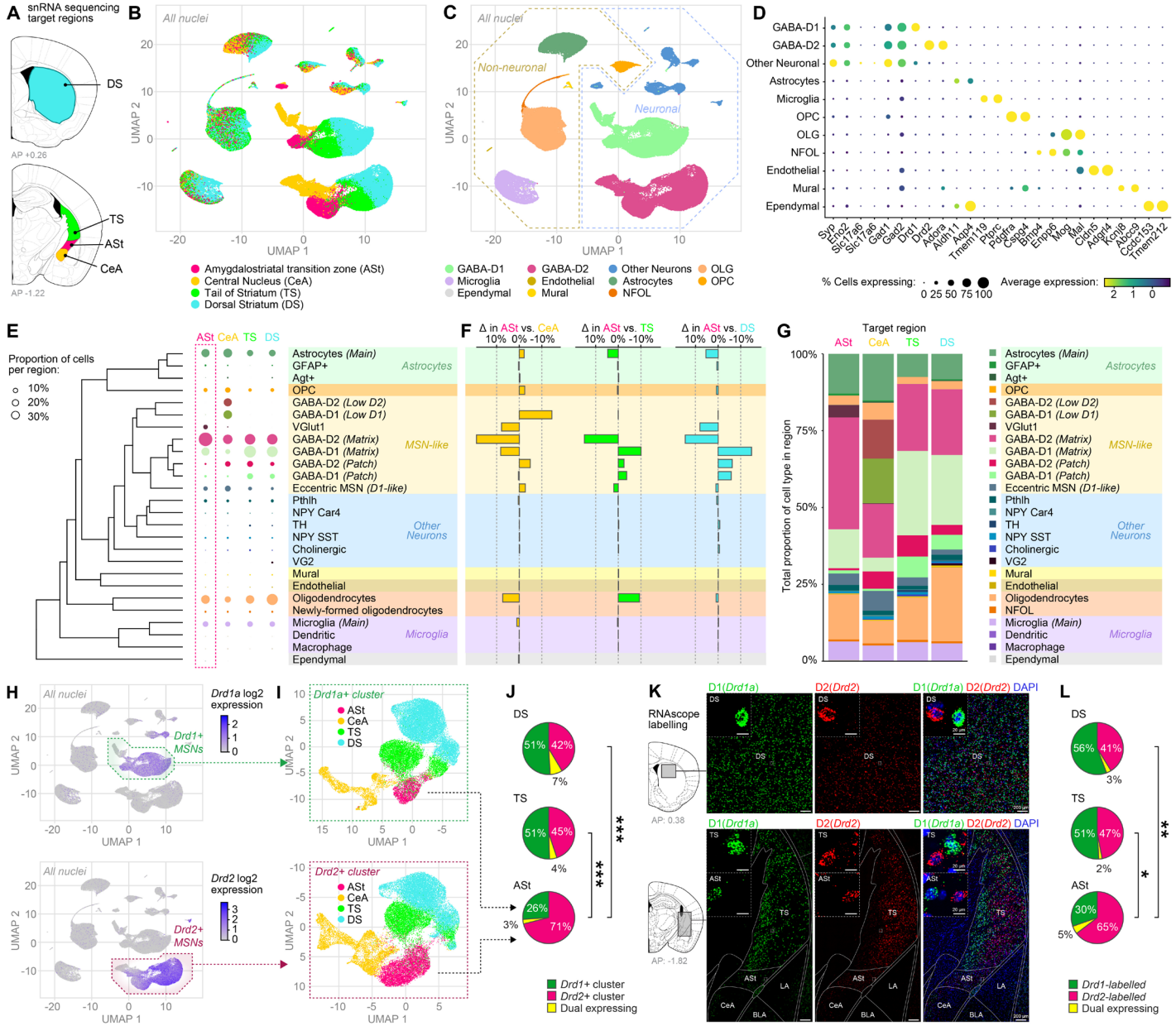

Figure 4

Figure 4. ASt cell-type composition is distinct from adjacent brain regions.
(**A**) Target regions for single-nucleus RNA sequencing (snRNA-seq).
(**B**) Two-dimensional non-integrated uniform manifold approximation projection (UMAP) of all sequenced nuclei passing quality filters (N = 97,434 nuclei, see also Figure S3), colored by region of origin.
(**C**) Two-dimensional UMAP, colored by broad cellular identity assigned by graph-based clustering of neuronal and non-neuronal cells.
(D) Cell-type-specific expression of canonical marker genes indicating broad cellular identity in the brain. Dot size is proportional to percentage of nuclei expressing the marker, with color scale representing normalized expression level.
(**E**) Dendrogram of cell type classification and proportion of cells of each class in the ASt and other target regions.
(**F**) Difference in overall proportion of each cell type between the ASt compared to the CeA, TS, and DS.
(**G**) Total proportion of cells of each identified type in each target region.
(**H**) All nuclei, colored by expression levels of *Drd1a* (top) or *Drd2* (bottom), with cells identified as part of the major *Drd1a*+ or *Drd2*+ clusters highlighted.
(**I**) *Drd1a*+ cluster (top) or *Drd2*+ cluster (bottom) neurons, with individual nuclei colored by region of origin.
(**J**) Relative proportion of nuclei classified in *Drd1a*+ or *Drd2*+ clusters in each striatal target region. Nuclei in the *Drd1a*+ cluster that also expressed *Drd2*, or in the *Drd2*+ cluster that expressed *Drd1a*, were classified as 'dual expressing'. *** $p < 0.001$.
(**K**) Representative images of *in situ* RNAscope labeling of *Drd1* RNA (green) and *Drd2* RNA (red) in striatal target regions.
(**L**) Relative proportion of cells in each target region positively labeled for *Drd1* RNA*, Drd2* RNA, or both ('dual expressing'). * $p < 0.05$, ** $p < 0.01$

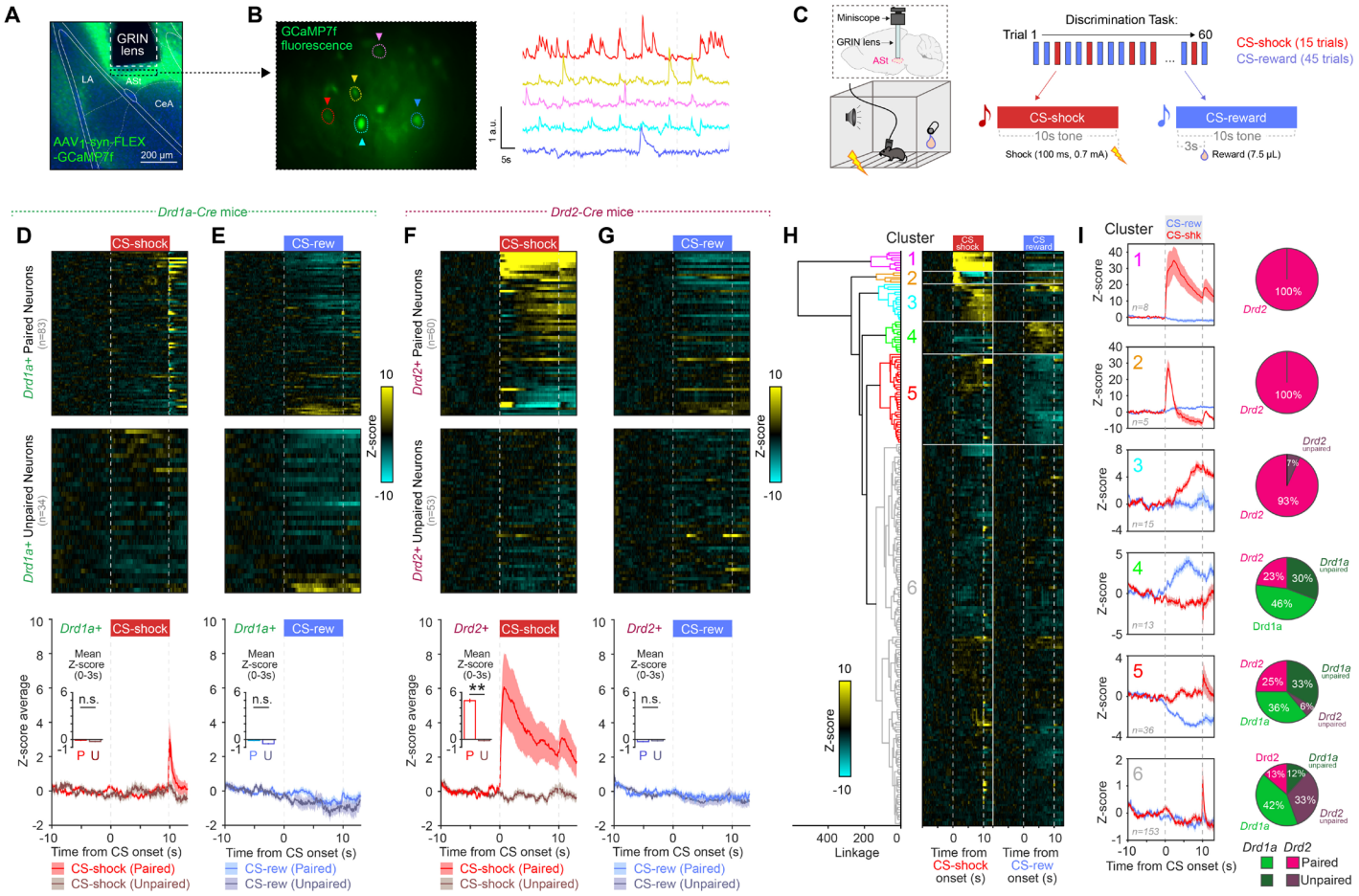

Figure 5. D2+ ASt neurons encode conditioned stimuli of negative valence

(**A**) GCaMP7f expression and lens targeting to ASt.
(**B**) Calcium imaging field of view and representative traces of fluorescence changes in individual neurons (dashed lines indicate concatenated trials).
(**C**) Two-tone discrimination task design parameters for *in vivo* calcium imaging of ASt neurons.
(**D and E**) *Drd1a*+ ASt neurons group average responses to CS-shock (**D**) and CS-reward (**E**) were not significantly different in paired group mice than unpaired controls.
(**F**) *Drd2*+ ASt neurons show greater conditioned responses to a shock-predicting cue ('CS-shock') in paired group mice than in unpaired controls (Two-tailed t-test, t = 3.135, df = 60, ** p < 0.01).
(**G**) *Drd2*+ ASt neuron group average responses to reward-predicting cue ('CS-reward') were not significantly different from unpaired controls.
(**H**) Agglomerative hierarchical clustering of calcium imaging responses of neurons from *Drd1a-Cre* and *Drd2-Cre* paired and unpaired groups.
(**I**) Mean z-score traces of responses to CS-shock and CS-reward (left) and proportion of neurons in each cluster from *Drd1a-Cre* and *Drd2-Cre* paired and unpaired groups (right) in each cluster. Clusters 1, 2 and 3, which feature robust responses to CS-shock, are dominated by neurons from the *Drd2-Cre* paired group. *Drd1a-Cre* paired group neurons are the largest proportion of clusters 4 and 5, which feature significant excitatory or inhibitory responses, respectively, to CS-reward.

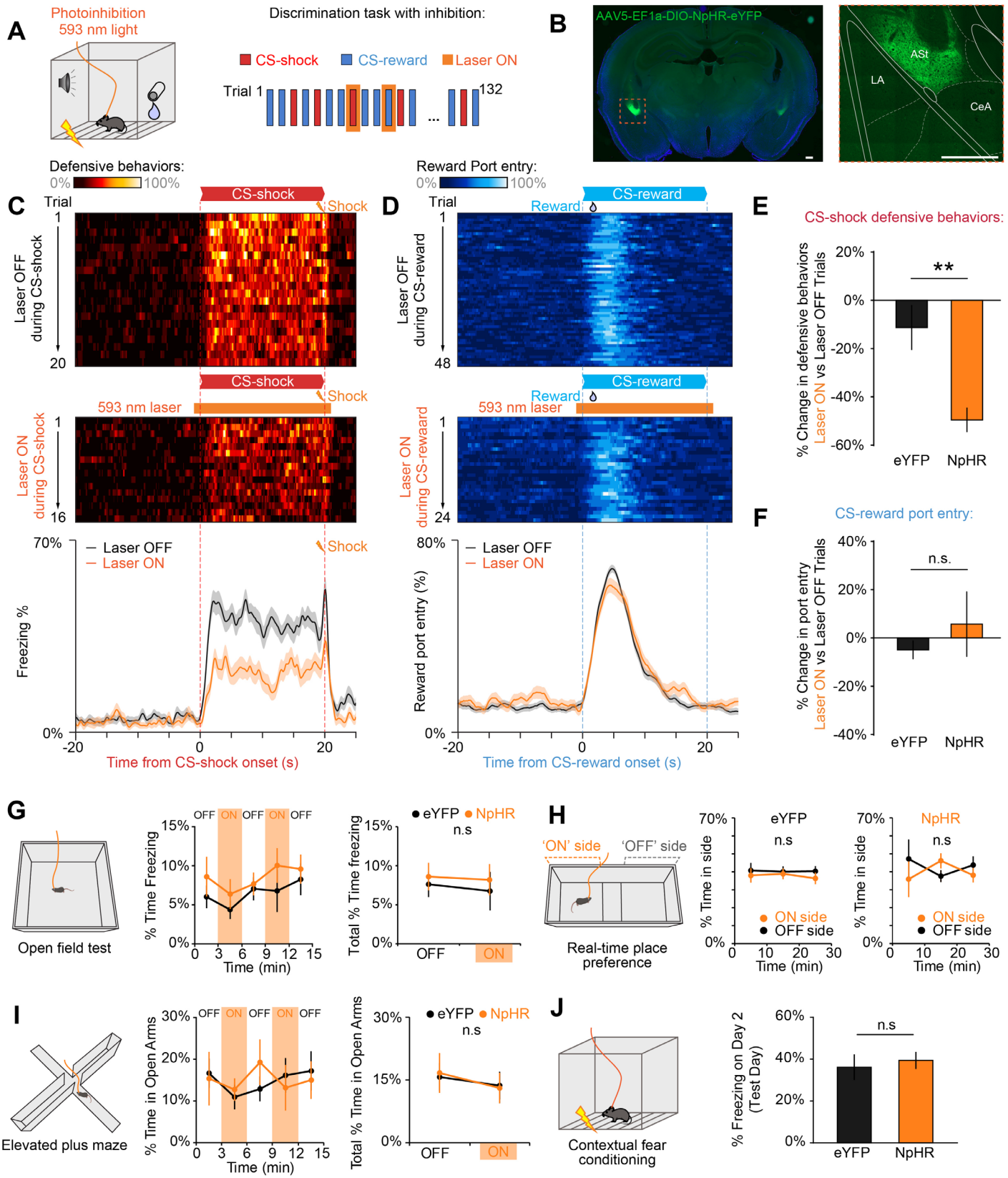

Figure 6

Figure 6. D2+ ASt neurons are necessary for the expression of fear responses to auditory cues, but conditioned reward responses or contextual fear conditioning.

(**A**) Behavioral paradigm for selective inhibition of D2+ ASt neurons during discrimination task. (**B**) Representative images of AAV-DIO-NpHR-eYFP expression in D2+ ASt neurons (Scale bars = 250 μm).
(**C**) Defensive behavior heatmaps during 'laser ON' (top) and 'laser OFF' trials (middle) and group averages (bottom) during CS-shock trials with and without photoinhibition.
(**D**) Port entry behavior heatmaps (top, middle) and group averages (bottom) during CS-reward trials with and without photoinhibition.
(**E**) Inhibition of D2+ ASt neurons resulted in a significantly greater reduction in conditioned defensive behaviors to CS-shock in NpHR mice compared with eYFP controls, and (**F**) had no effect on port entry during CS-reward (*$p < 0.05$, Student's t-test, N=8 mice NpHR, 9 mice eYFP).
(**G**) Optogenetic inhibition of D2+ ASt neurons had no effect on overall locomotion in an open field maze task (N=5 mice NpHR, 10 mice eYFP).
(**H**) Inhibition of D2+ ASt neurons did not cause preference or aversion for an area paired with inhibition in a real-time place preference task (N=5 mice NpHR, 10 mice eYFP).
(**I**) Inhibition of D2+ ASt neurons caused no overall changes in exploration of open arms in an elevated plus maze (N=5 mice NpHR, 10 mice eYFP).
(**J**) Inhibition of D2+ ASt neurons on day 2 of a contextual fear conditioning task had no effect on contextual freezing (N=5 mice NpHR, 9 mice eYFP).

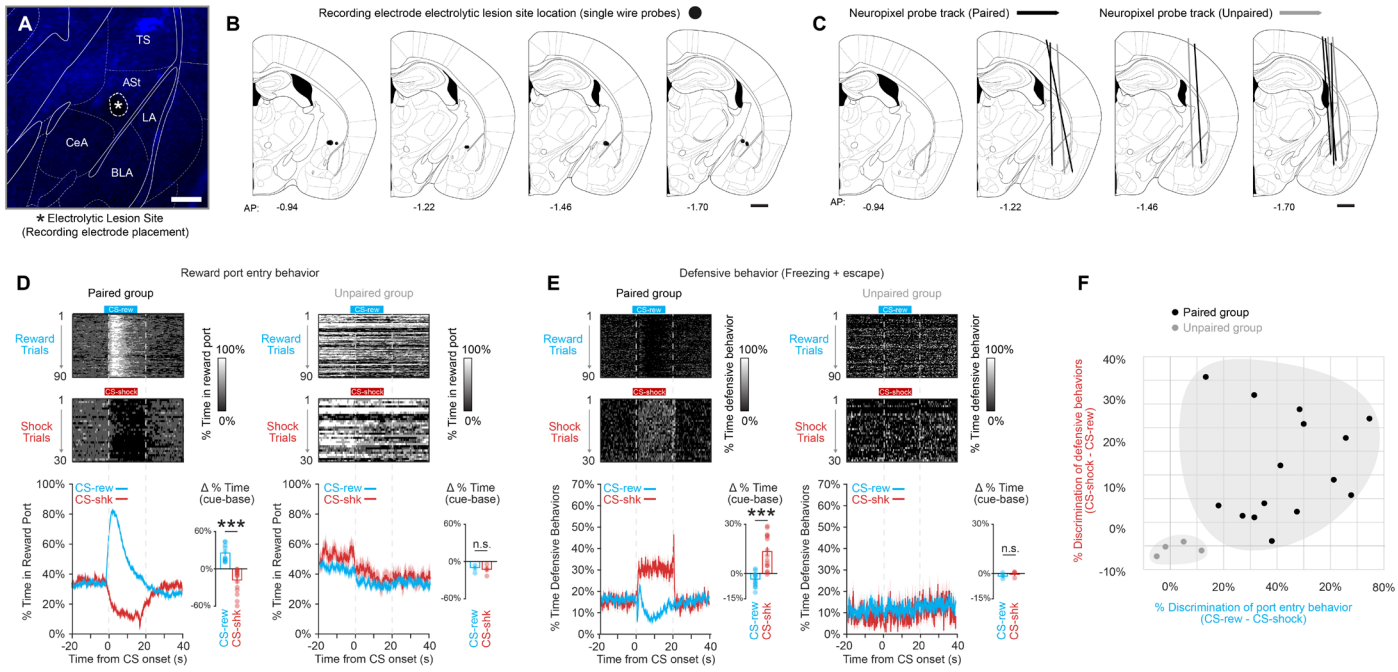

Figure S1. Histological targeting and behavioral validation for *in vivo* electrophysiology recordings.
(**A**) Representative image of electrolytic lesion site to confirm recording electrode targeting to the ASt (Blue = DAPI, Scale bar = 100 µm).
(**B**) Histologically verified lesion sites of single-wire electrode placements in recording experiments targeting ASt.
(**C**) Histologically verified probe tracks of Neuropixels probes in recording experiments.
(**D-F**) Validation of conditioned behavioral responses during two-tone discrimination task in mice in electrophysiological recording experiments (N=15 mice paired, 4 mice unpaired). Paired group mice showed distinct responses to the CS-shock and CS-reward tones in reward port entry behavior (Two-tailed t-test, t = -9.204, df = 14, *** p = $2.584e^{-07}$) (**D**) and defensive responses (Two-tailed t-test, t = 5.927, df = 14, *** p = .000018) (**E**), consistent with successful discrimination between the two tones compared with unpaired mice (**F**).

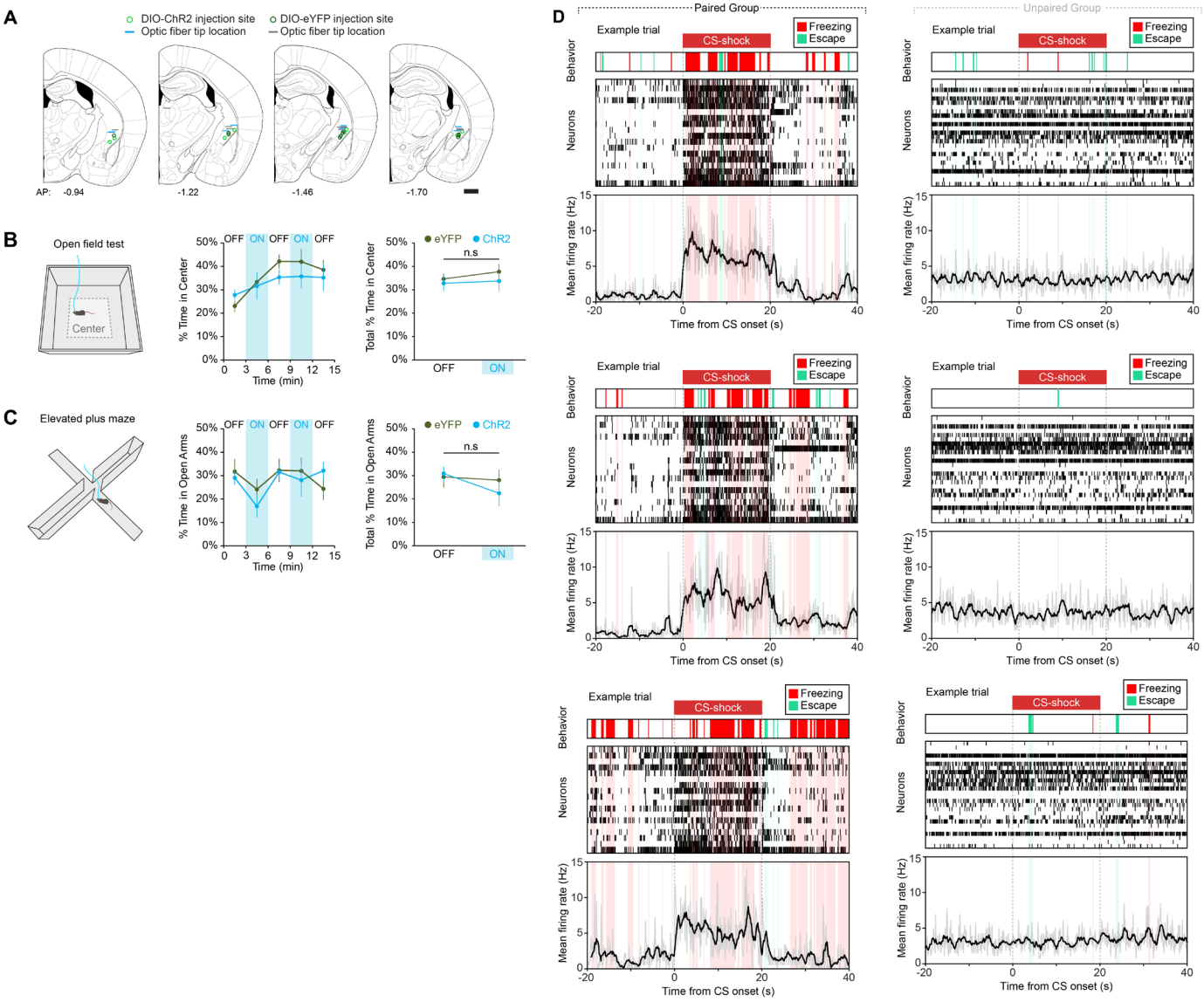

Figure S2. Optogenetic activation of ASt neurons does not affect anxiety-related behaviors.

(**A**) Histologically verified optic fiber implant locations and viral injection sites for AAV-DIO-ChR2-eYFP and AAV-DIO-eYFP controls in optogenetic excitation experiments targeting ASt neurons in VGAT:Cre mice.
(**B**) Optogenetic activation of ASt neurons does not affect time in center of an open field arena.
(**C**) Optogenetic activation of ASt neurons does not affect time spent in open arms of an elevated plus maze. N=8 mice ChR2, 10 mice eYFP.
(**D**) Additional representative trials from discrimination task experiments showing simultaneous subsecond behavior, neural spikes, and average neuron firing rate during presentation of CS-shock.

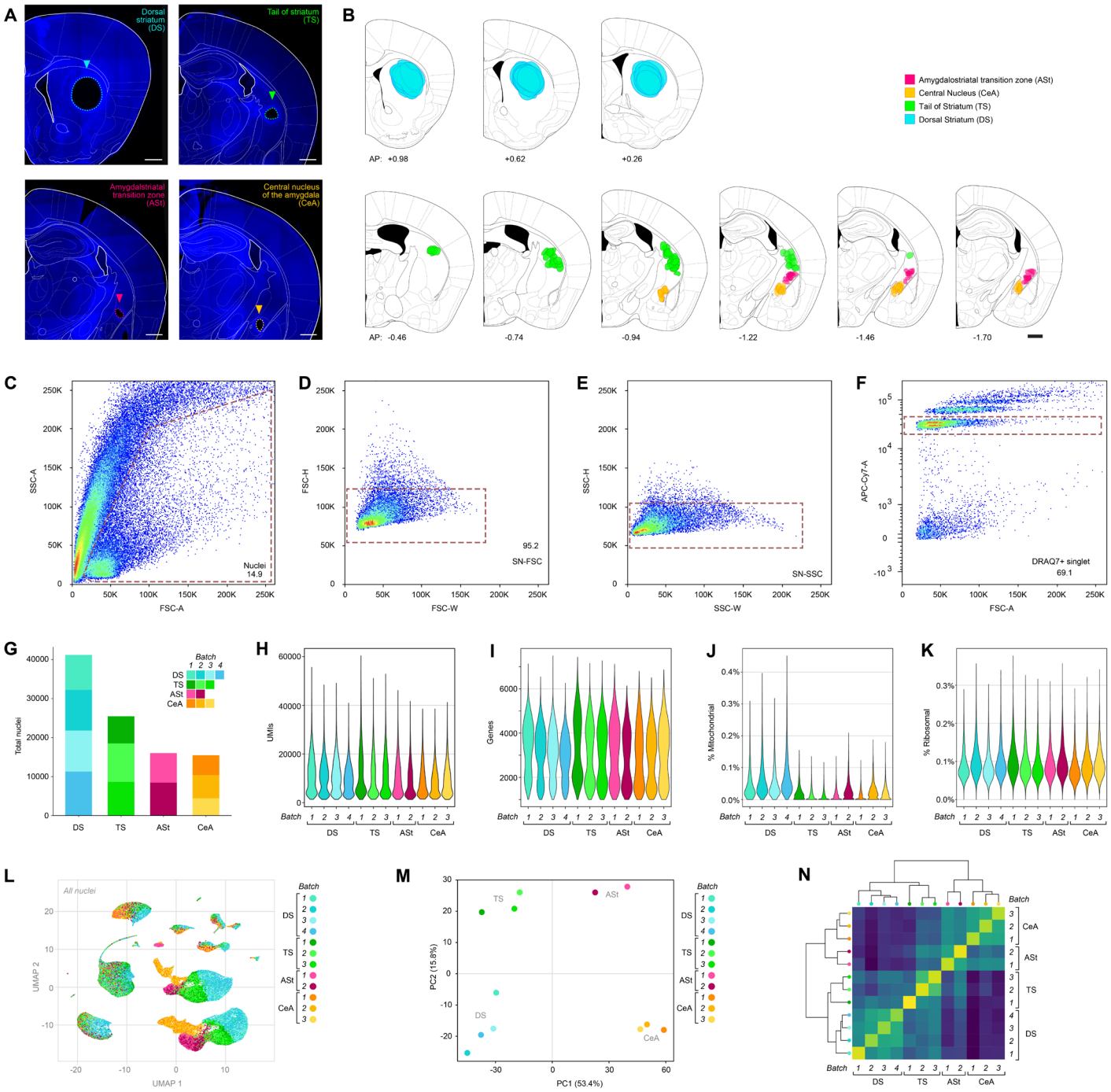

Figure S3

Figure S3. Quality control metrics for single-nucleus RNA sequencing

(**A**) Representative images of tissue microdissection sites from RNA sequencing target regions, the dorsal striatum (DS), tail of striatum (TS), amygdalostriatal transition zone (ASt), and central nucleus of the amygdala (CeA) (Blue = DAPI, scale bars = 500 μm).
(**B**) Location of all tissue sample sites used for single-nucleus RNA sequencing, color coded by region. AP = anteroposterior distance from bregma (mm), scale bar = 500 μm.
(**C-F**) Density plots outlining the gating strategy for FANS isolation of single nuclei. Nuclei isolated from regions of interest were FANS sorted using 70 μm nozzle at 52 psi. Nuclei were sorted based on size (**C**), duplicates and/or morphology (**D, E**), and by high DRAQ7 signal, which stains DNA in nuclei (**F**). Single DRAQ7$^+$ events at the lowest stoichiometric fluorescence multiple were considered nuclei.
(**G**) Absolute number and proportion of nuclei passing quality control filters from each batch in each region.
(**H**) UMIs detected per nucleus, filtered at the median per library + five times the median absolute deviation.
(**I**) Genes detected per nucleus, filtered at minimum 1000 genes.
(**J**) Percent mitochondrial reads per nucleus, filtered at median per library + five times the median absolute deviation.
(**K**) Percent ribosomal reads per nucleus, no quality filter applied.
(**L**) PCA of pseudobulk samples created from each batch, colored by both target region and batch identity.
(**M**) UMAP of all sequenced nuclei colored by both target region and batch identity.
(**N**) Evaluation of transcriptional homology on a per-batch basis, where the distance matrix is based on Spearman correlation between median expression of genes on a per-region basis, and the dendrogram was created via hierarchical clustering on this correlation matrix.

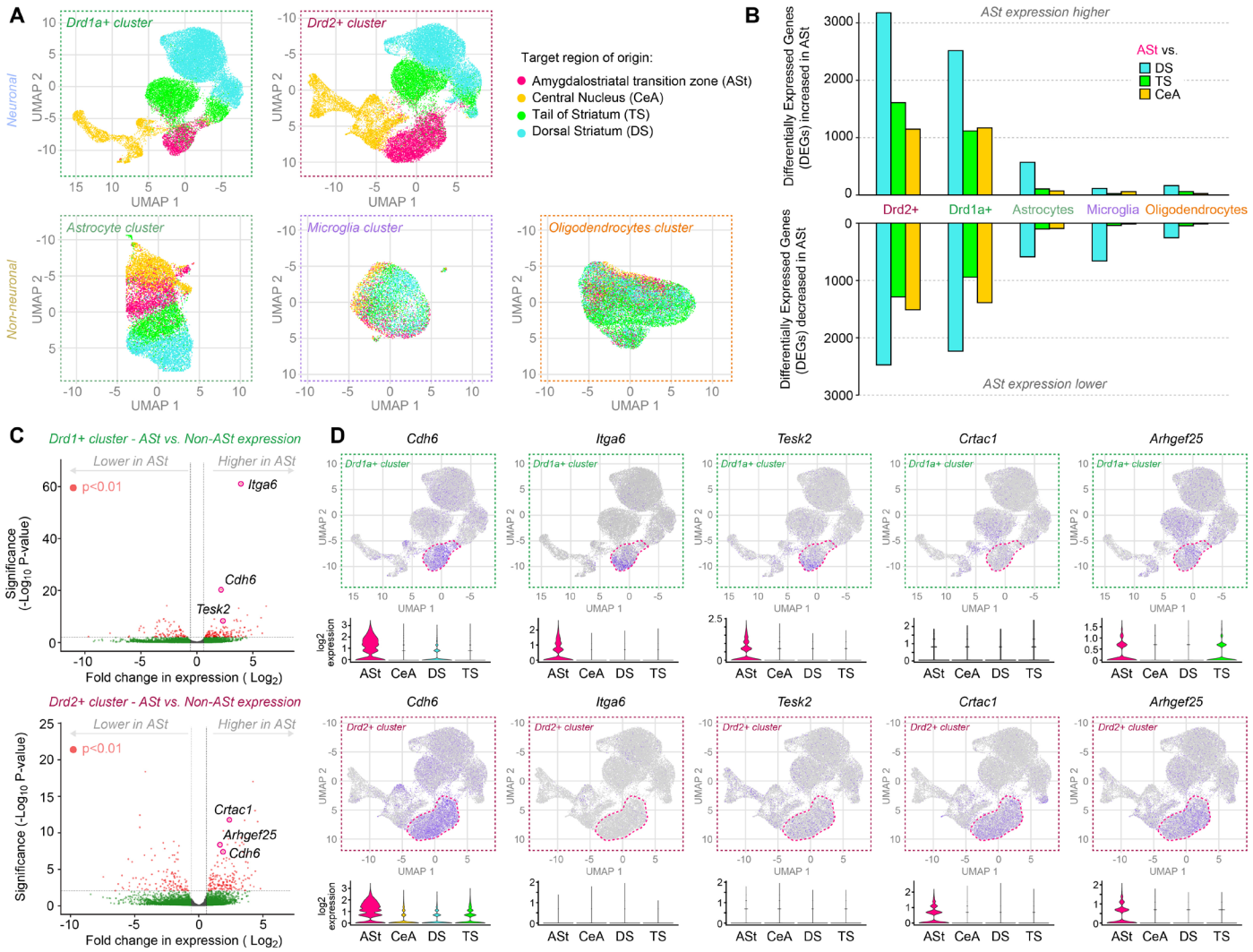

Figure S4. Single-nucleus RNA sequencing identifies unique transcriptomic signatures for ASt cells.

(**A**) UMAP projections of nuclei from the largest cell type clusters (*Drd1a*+, *Drd2*+, Astrocytes, Microglia and Oligodendrocytes) colored by tissue region of origin.
(**B**) Number of differentially expressed genes ($p < 0.01$, 1.5 log-fold change) with increased expression (top) or decreased expression (top) in ASt nuclei relative to nuclei from the central nucleus of the amygdala (CeA), tail of striatum (TS) and dorsal striatum (DS) within each cell type cluster.
(**C**) Volcano plot showing differentially expressed genes between ASt and non-ASt nuclei in *Drd1*+ cluster (top) and Drd2+ cluster (bottom). Dashed lines indicate $p < 0.01$ and a fold-change of 1.5. Dots colored grey fail to meet ether standard, dots colored green have sufficient fold change but not significance, while red dots meet both standards. Marker genes of interest for further analysis are circled.
(**D**) Expression of specific marker genes of interest in *Drd1*+ cluster (top) and Drd2+ cluster (bottom) neurons. Expression is visualized via UMAP and violin plot. UMAP expression is colored based on increasing normalized expression intensity. Violin plots show smoothed expression density, colored and split based on regional identity within each cluster.

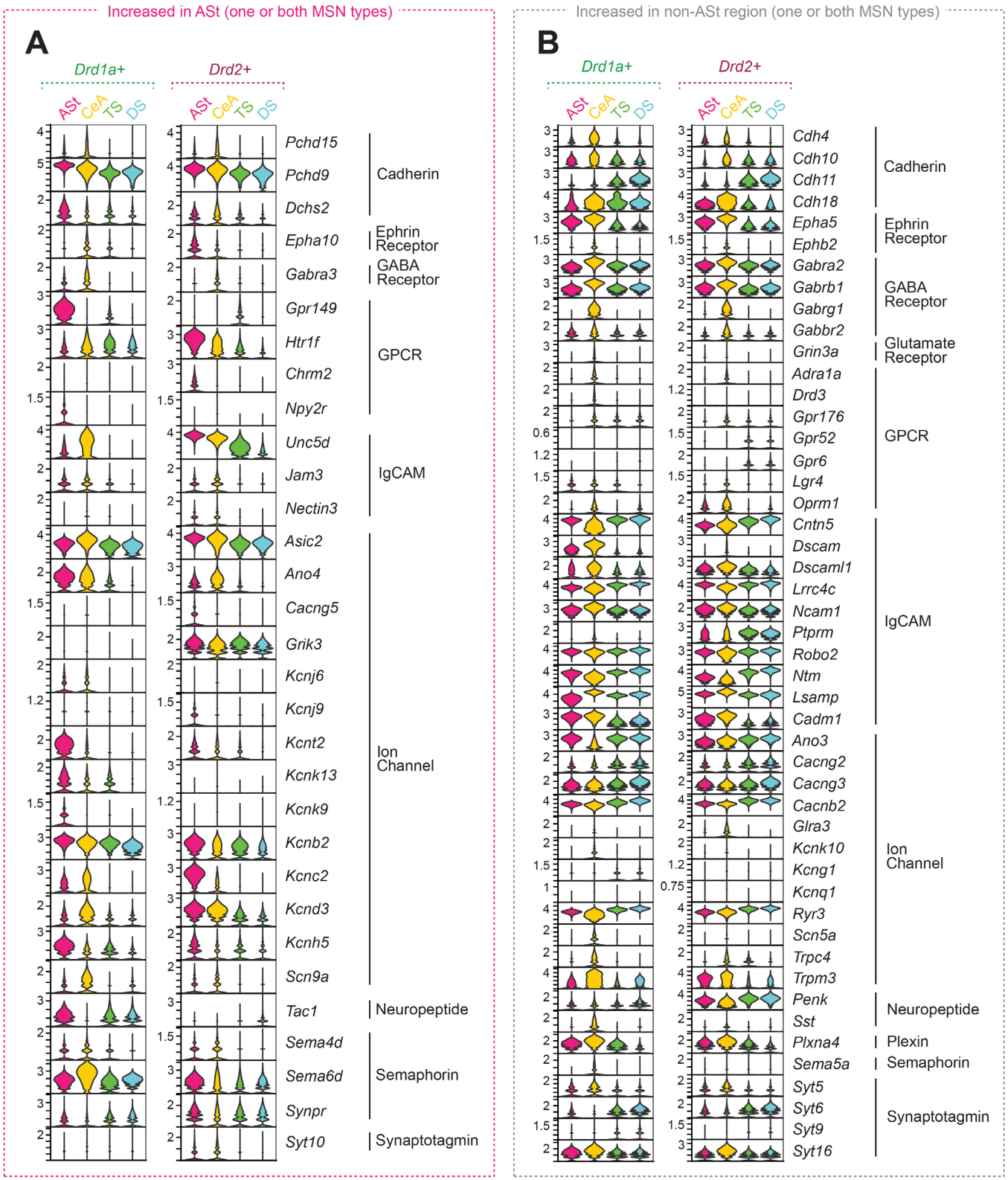

Figure S5. Differentially expressed genes of interest with neurologically-relevant function in striatal subregions of interest.

(**A**) Differentially expressed genes with increased expression in ASt falling into predefined HGNC gene families related to neurological function, increased in *Drd1a*+ and/or *Drd2*+ MSNs.
(**B**) Differentially expressed genes with increased expression in batched non-ASt regions (DS, TS, and/or CeA) falling into predefined HGNC gene families related to neurological function, increased in *Drd1a*+ and/or *Drd2*+ MSNs.

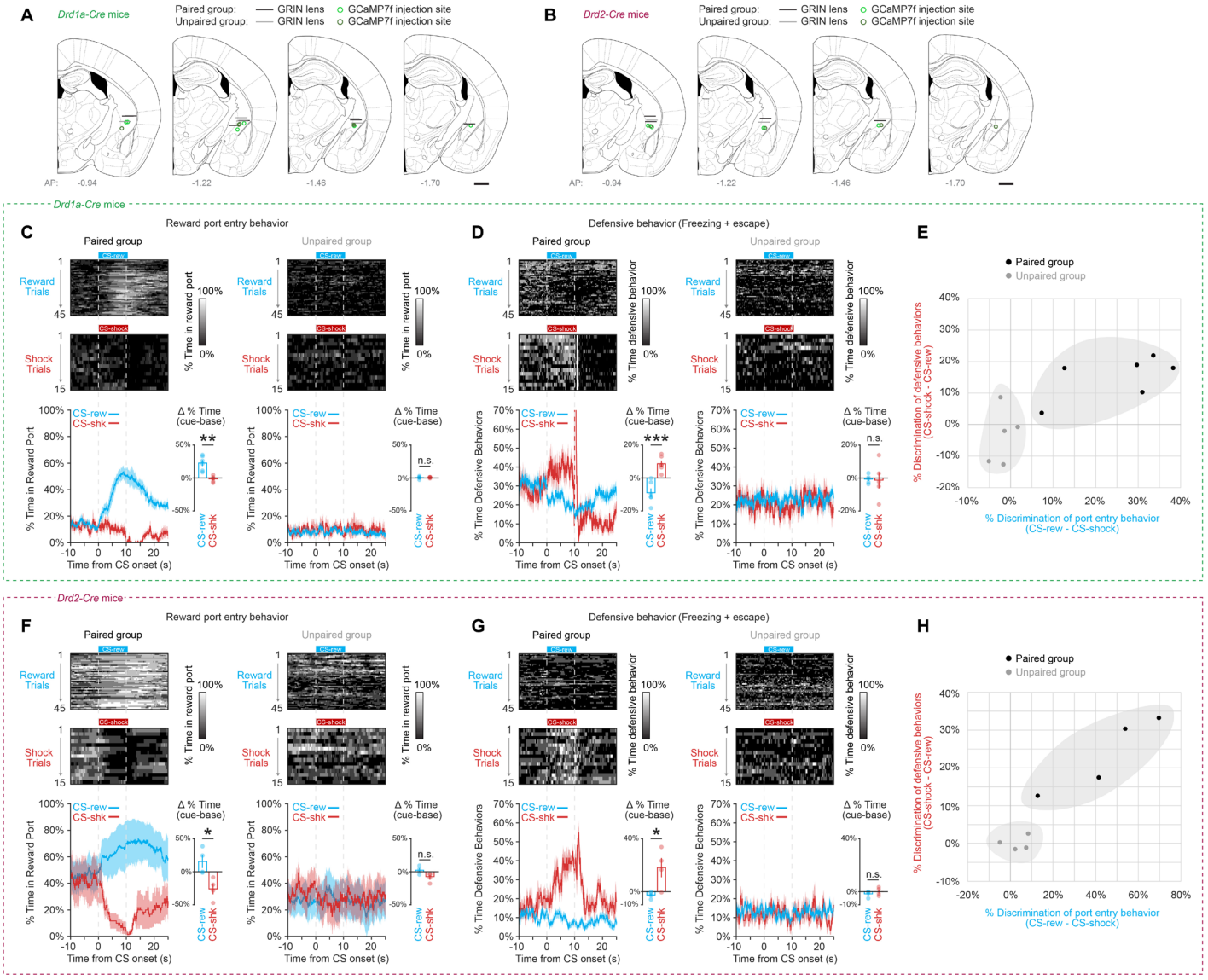

Figure S6. Targeting of ASt neurons and behavioral validation for *in vivo* calcium imaging.
(**A-B**) Histologically verified GRIN lens implant locations and AAV1-Syn-FLEX-GCaMP7f viral injection sites in recording experiments targeting *Drd1a*+ neurons (**A**) and *Drd2*+ neurons (**B**) in the ASt.

(**C-E**) Validation of conditioned behavioral responses during two-tone discrimination task in *Drd1a-Cre* mice (N=6 mice paired, 5 mice unpaired). Paired group mice showed distinct responses to the CS-shock and CS-reward tones in reward port entry behavior (Two-tailed t-test, t = 5.0019, df = 5, *** p < 0.0038) (**C**) and defensive responses (Two-tailed t-test, t = 5.2045, df = 5, *** p = 0.0035) (**D**), consistent with successful discrimination between the two tones compared with unpaired mice (**E**).

(**F-H**) Validation of conditioned behavioral responses during two-tone discrimination task in *Drd2-Cre* mice (N=4 mice paired, 4 mice unpaired). Paired group mice showed distinct responses to the CS-shock and CS-reward tones in reward port entry behavior (Two-tailed t-test, t = 3.5442, df = 3, * p = 0.0382) (**F**) and defensive responses (Two-tailed t-test, t = 4.7145, df = 3, * p = 0.0181) (**G**), consistent with successful discrimination between the two tones compared with unpaired mice (**H**).

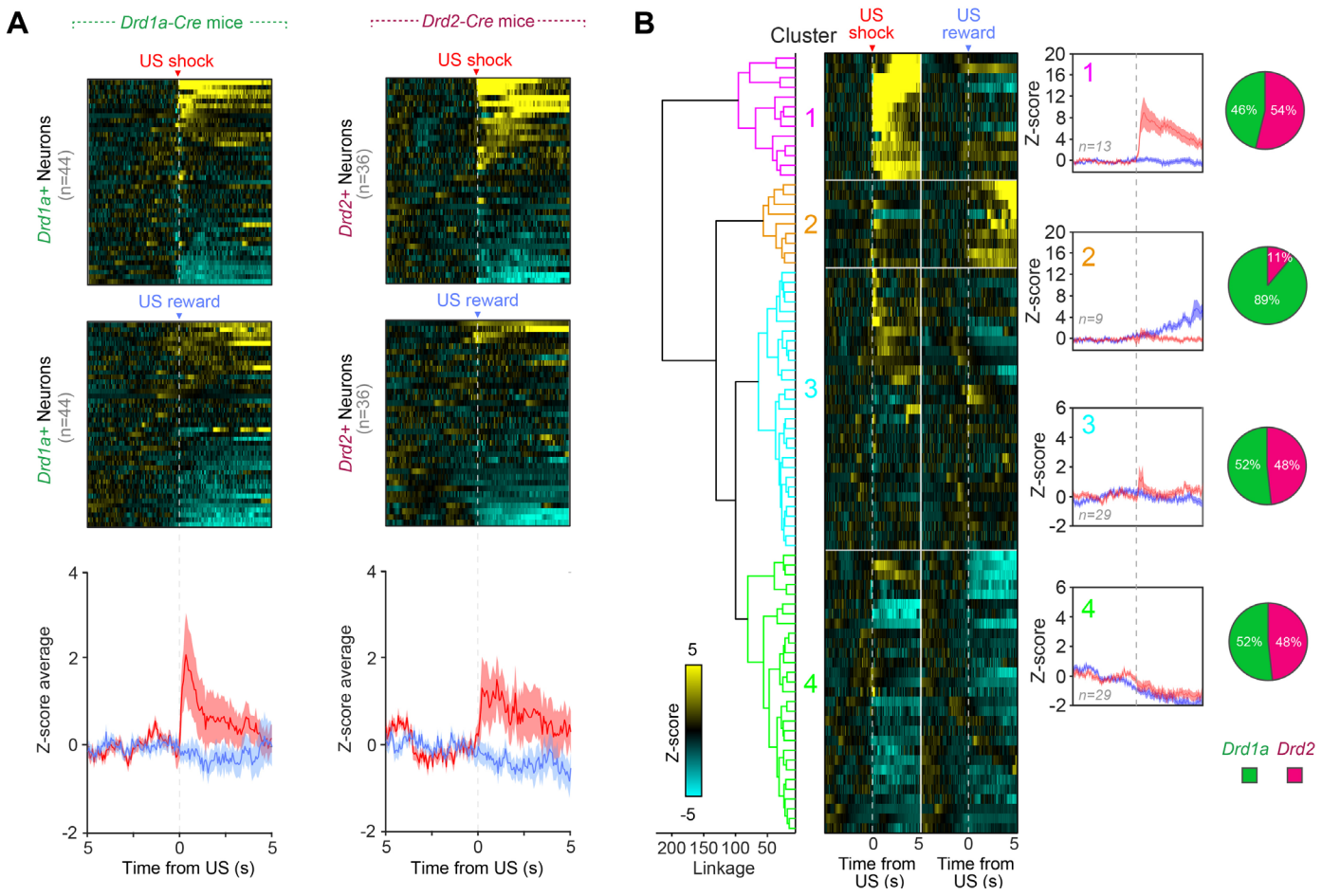

Figure S7. ASt neuron responses to aversive and rewarding unconditioned stimuli.
(**A**) Individual neuron (top) and group average traces (bottom) of Z-score changes in GCaMP7f fluorescence in response to presentation of an aversive US (0.7 mA foot shock) or consumption of a rewarding US (7.5 uL chocolate Ensure™).
(**B**) Agglomerative hierarchical clustering of calcium imaging responses to each US of neurons from *Drd1a-Cre* and *Drd2-Cre* mice. *Drd1a*+ and *Drd2*+ neurons both responded to CS shock, but a subcluster of reward-responsive neurons was predominantly composed of *Drd1a*+ neurons.

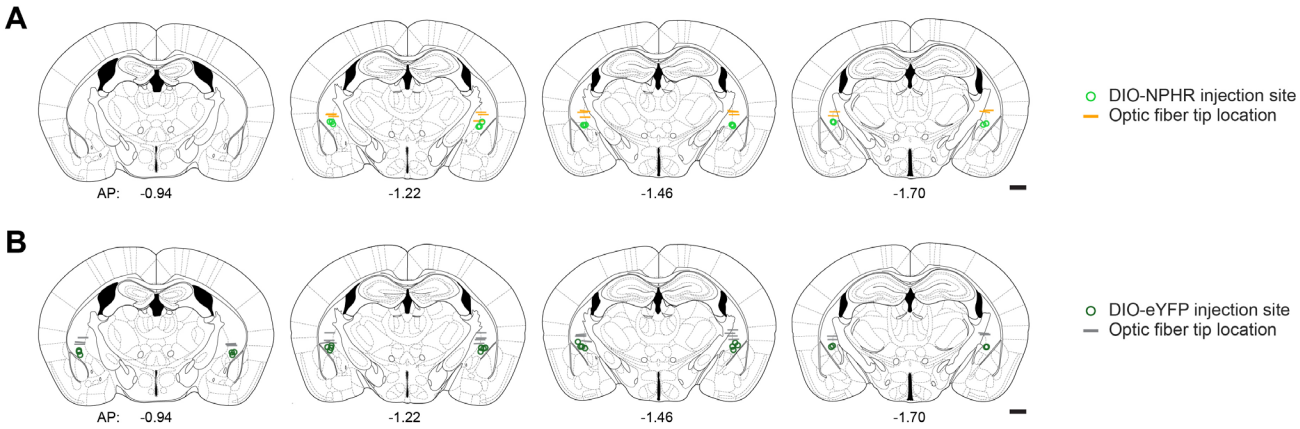

Figure S8. Targeting of *Drd2*+ ASt neurons and for optogenetic inhibition.
(**A-B**) Histologically verified optic fiber implant locations and injection sites of (**A**) AAV-DIO-NpHR-eYFP group mice and (**B**) AAV-DIO-eYFP control group mice in optogenetic inhibition experiments targeting *Drd2*+ ASt neurons. Scale bars = 500 μm.

ACKNOWLEDGEMENTS:

We thank Chris Leppla, Praneeth Namburi, and Kanha Batra for their contributions to the project. We also thank Alcino Silva, Peyman Golshani, Daniel Aharoni, Tristan Shuman, and Denise Cai for their assistance and contributions to UCLA Miniscope resources used in the project. K.M.T. is an HHMI Investigator and the Wylie Vale chair at the Salk Institute for Biological Studies and this work was supported by funding from the JPB Foundation, the PIIF, PNDRF, JFDP, New York Stem Cell Foundation, Klingenstein Foundation, McKnight Foundation, The Salk Institute, Howard Hughes Medical Institute, Clayton Foundation, Kavli Foundation, Dolby Family Fund, R01-MH115920 (NIMH), R37-MH102441 (NIMH), the NIH Director's New Innovator Award DP2-DK102256 (NIDDK) and Pioneer Award DP1-AT009925 (NCCIH). F.M. was supported by a CIHR Postdoctoral Fellowship and a K99/R00 NIH Pathways to Independence Award (K99 MH121563). H.L. was supported by a K99/R00 NIH Pathways to Independence Award (K99 DA055111-01). S.S. was supported by China Scholarship Council grant 201806010370.

AUTHOR CONTRIBUTIONS

Conceptualization, F.M. and K.M.T.;
Methodology, K.M.T., F.M., J.R.H.;
Investigation, F.M., C.R.L., J.R.H., H.L., S.S., M.N.K., M.E.L, R.W., H.S.C., M.B., R.R.P., A.L.G.,
Formal Analysis, F.M., C.R.L., J.R.H., H.L., S.S., M.N.K., M.E.L, L.R.K., F.H.T, M.B., A.L.G., J.D., C.C., L.M., T.D.P.;
Writing, F.M., J.R.H., M.N.K., K.M.T.;
Supervision, F.M., R.W., T.D.P., M.K.B., C.M.R., K.M.T.;
Funding Acquisition, F.M., T.D.P., M.K.B., C.M.R., and K.M.T.;

DECLARATION OF INTERESTS
The authors declare no competing interests.

RESOURCE AVAILABLITY

Lead Contact

Further information and requests for resources and reagents should be directed to and will be fulfilled by the Lead Contact, Kay Tye (kaytye@salk.edu).

Materials Availability

This study did not generate new unique reagents.

Data and code availability

Single nucleus RNA-seq data have been deposited at GEO: GSE211437. All code and data that support the findings of this study are available upon request to the lead contact.

EXPERIMENTAL MODEL AND SUBJECT DETAILS

Adult, 8-12 week old, wild-type C57BL6J mice (RRID:IMSR_JAX:000664), DRD1-Cre mice (RRID:MMRRC_036089-UCD), DRD2-Cre mice (RRID:MMRRC_036089-UCD), and VGAT-Cre mice (RRID:IMSR_JAX:028862) were used in all experiments as stated in the text. Mice were housed in the Salk Institute of Biological studies on a 12-h reverse light/dark cycle with ad libitum access to food and water except when otherwise stated in experimental procedures. All experiments were conducted during the dark cycle phase. All experimental procedures were carried out in accordance with NIH guidelines and approval of the Salk Institutional Animal Care and Use Committee.

METHODS DETAILS

Stereotactic surgery procedures

All surgeries were conducted under aseptic conditions. Mice were anesthetized with an isoflurane/oxygen mixture (4-5% for induction, 1-2% for maintenance) and placed in a stereotaxic head frame (David Kopf Instruments, Tujunga, CA, USA). A heating pad was placed beneath the mice to maintain body temperature, and Sterile Lubricant Eye Ointment (Stye, INSIGHT Pharmaceuticals Corp. Langhorne, PA) was applied to the eyes to prevent drying. An incision was made along the midline to expose the skull and a dental drill was used to perform a craniotomy. During all surgeries, animals were injected subcutaneously with 1 mL of Ringer's solution, Buprenorphine (1 mg/kg), and Meloxicam (5 mg/kg). For recovery animals were placed in a clean cage on a heating pad. Animals were given >7 days of recovery period before being subjected to behavioral paradigms.

Stereotaxic coordinates were measured relative to bregma. Coordinates for injections targeting Amygdalostriatal transition zone (ASt) were +/- 3.17 ML (mediolateral), -1.52 mm AP (anteroposterior), and -4.28 mm DV (dorsoventral) relative to bregma. All injections of viral vectors were performed using glass pipettes (Drummond Scientific) pulled to a 130-140 µm tip diameter with a pipette puller (Narishige PC-10, Amityville, NY, USA). Pipettes were either attached to 10 µL microsyringes (Hamilton Microlitre 701, Hamilton Co., Reno, NV, USA) with a microsyringe pump (UNP3; WPI, Worcester, MA, USA) and digital controller (Micro4; WPI, Worcester, MA, USA), or to the Nanoject III Programmable Nanoliter Injector (Drummond Scientific, Broomall, PA, USA) with digital controller (Drummond Scientific, Broomall, PA, USA). For each injection, micropipettes were slowly lowered to the target site and viral vectors were delivered at a rate of 0.1-5.0 nL per second. The pipette was then slowly raised 0.02 mm and left in place for 15-20 min to allow diffusion of the virus, then slowly withdrawn.

Surgery for in vivo Electrophysiology

An electrode consisting of a bundle of 16 single nichrome wires of 9 µm diameter (Stablohm 675, CFW Material #: 100-188, California Fine Wire Company, Grover Beach, CA, USA) was implanted unilaterally in the ASt. Electrodes were lowered into the brain at a rate of 0.01 mm/s. Electrodes were secured with C&B-Metabond Quick adhesive Luting Cement (Parkell, Long Island, NY, USA) and dental cement (Ortho-Jet powder, Lang Dental, Wheeling, IL, USA). Two to three skull screws (00-96 x 1/16 (stainless steel) 1.6mm cut length, Plastics One) were secured in the skulls around the implanted electrode, with a layer of C&B-Metabond Quick adhesive Luting Cement and dental cement for stabilization. For additional *in vivo* electrophysiology experiments, animals were implanted with Neuropixels probes. Neuropixels probes (Version 1.0) were assembled into a custom made 3D printed probe holder prior to implantation. Before surgery, the probe shank was soaked in 70% ethanol for 20 minutes. The petroleum jelly was gently applied around the base of the probe shank to form a hermetic seal. The remaining length of the probe shank was dipped into a fluorescent DiI (Vybrant DiI Cell-Labeling Solution, Waltham, MA, USA). For implantation, the probe holder with the probe was attached to a stereotaxic arm and centered at ML ± 3.17 mm, AP -1.52 mm relative to bregma. The probe was then lowered to DV -5.00 mm relative to bregma at a rate of 0.01 mm/s.

Surgery for Optogenetic Manipulations

For optogenetic stimulation experiments mice received unilateral injections of 50 nL AAV_5-DIO-ChR2-eYFP in the ASt. For optogenetic inhibition experiments, mice received bilateral injections of 50 nL AAV_5-DIO-NpHR-

eYFP in the ASt. For both experiments a 300-µm diameter optic fiber (0.37 numerical aperture) encased in a 1.25 mm ferrule was then implanted with the fiber tip 0.30 mm above the injection site. Identical parameters were used for the non-opsin controls except the viral vector injected was AAV_5-DIO-eYFP.

Surgery for *in vivo* Calcium Imaging

For calcium imaging experiments, 50 nL of AAV1-Syn-FLEX-GCaMP7f was injected in the ASt at a rate of 1 nL per second. Following injection, a 0.5 mm x 6.1 mm 0.5 pitch gradient refractive index (GRIN) lens (Inscopix Inc, Mountain View, CA, USA) was centered over the injection site and lowered to a depth 0.05 mm above the injection site at a rate of 0.01 mm/s. On the contralateral side, a screw (00-96 x 1/16 (stainless steel) 1.6mm cut length, Plastics One) was secured into the skull. Both the lens and the skull screw were secured with super glue (Krazy Glue All Purpose, The Original Super Glue Corporation, Ontario, CA, USA) and dental cement (Ortho-Jet powder, Lang Dental). A small platform flush with the GRIN lens was created with dental cement, and a plastic cover fixed over the GRIN lens with dental cement to prevent damage to the lens prior to securing the baseplate. Approximately 4 weeks following implantation, a 1.8 mm objective 0.25 pitch GRIN lens (Edmund Optics, Barrington, NJ, CA) was placed over the GRIN lens with dental cement at a height resulting in the optimal focal plane. A small baseplate (miniscopeparts.com) was then secured to the previously formed dental cement.

Electrode Construction

For recording single-unit activity, multi-electrode arrays were constructed. Arrays consisted of one multi-channel single wire probe, using Super Glue Corporation (Omnetics Connector Corp., Minneapolis, MN) as the structural component. This array was connected directly to the plug using a plastic spacer. The array was comprised of 16 single wires (Stablohm 675, CFW Material #: 100-188, California Fine Wire Company, Grover Beach, CA). Wires were aligned using the length of syringe needle (2-3 mm). The wire insulation was then stripped using forceps and wires were connected to the Omnetics connector using a conductive adhesive (Super Shield Silver Conductive Paint; MG Chemicals, Burlington ON). Super glue and epoxy were used to ensure connections were secure. Serrated tungsten scissors (Fine Science Tools, Foster City, CA) were used to cut the arrays to length. A 50/50 gold plating solution consisting of gold solution (Neuralynx, Bozeman, MT) and 1 µM polyethylene glycol was then applied to decrease the impedance of the wires to 150-250MΩ. Finally, a low impedance bare silver wire (California Fine Wire, Grover Beach, CA) was soldered to the last pin on the connector, and then the connection was covered with dental cement.

Behavioral Tasks

All behavioral tasks involving optogenetic manipulation or calcium imaging were performed 6-8 weeks after injection of viral vectors to allow sufficient expression of opsins or genetically-encoded calcium indicators. For at least four days prior to behavioral experiments mice were habituated to experimenter handling and attachment of optic fiber patch cables to surgically implanted optic fibers or tethers for calcium imaging and electrophysiology recordings. All behavioral experiments except the discrimination task were analyzed using Ethovision XT software (Noldus, Wagenigen, Netherlands) and recorded with a digital video camera above the test arena.

Open Field Test

Mice were placed in a 53 x 50 cm arena with four transparent plexiglass walls, and allowed to move freely throughout the arena for 15 min. Light stimulation was delivered during the 3-6 min and 9-12 min epochs (ChR2 mice and eYFP controls: 10 mW 473 nm light at 20Hz, 5 ms pulse width. NpHR mice and eYFP controls: 3 mW 593 nm light, constant delivery). Overall locomotion and time spent in edges (50% of arena area closest to walls) and center region of arena during each epoch was analyzed for each mouse.

Elevated Plus Maze

Mice were placed in the center of the elevated plus maze (EPM) apparatus, consisting of two open arms (30 x 5 cm) and two enclosed arms (30 x 5 x 30 cm) extending from the center platform (5 x 5 cm). The entire apparatus was elevated 75 cm from the floor. Mice were given 1-5 min to recover from handling before the 25 min testing phase began. Light stimulation was delivered during the 5-10 min and 15-20 min epochs (ChR2 mice and eYFP controls: 10 mW 473 nm light at 20Hz, 5 ms pulse width. NpHR mice and eYFP controls: 3

mW 593 nm light, constant delivery), and time spent in open and closed arms of the apparatus throughout each epoch was quantified.

Real-Time Place Preference

Mice were placed in the center of a transparent Plexiglass chamber (57.15 x 22.5 x 30.5 cm). The chamber was divided into 'ON side' and 'OFF side' compartments (counterbalanced between and within groups). The chamber was then illuminated with 30 lux ambient light. Mice were allowed to freely explore the chambers for 30 min during which entry into the 'ON side' triggered photostimulation (ChR2 mice and eYFP controls: 10 mW 473 nm light at 20Hz, 5 ms pulse width. NpHR mice and eYFP controls: 3 mW 593 nm light, constant delivery) until the side was exited, and total time spent in each side throughout the task was quantified.

Two-tone Discrimination Tasks

Animals were trained and tested in standard operant chambers (23 x 30 x 40 cm; Med Associates inc.) within a sound attenuating cubicle. Each chamber was equipped with speakers for tone delivery, a syringe pump for reward delivery, a reward port with an infrared beam to detect port entries, a grid floor for shock delivery, infrared house lights and a camera for behavioral recording.

Prior to discrimination training, mice were sequentially trained to recognize reward-predicting and shock-predicting cues. On all tasks with rewards, mice were food-restricted (3.0 g food per mouse per day) prior to testing. In the first phase of training animals were trained to associate a conditioned stimulus ('CS-reward') with delivery of a high-calorie reward (Ensure™, Abbott Laboratories). During reward conditioning animals were presented with 60 trials in which a pure auditory tone cue of (20 kHz or 3.5 kHz, counterbalanced) predicted the delivery of a Ensure reward (7.5 µL per trial) to the reward port. Collection of the reward prior to the end of the tone resulted in termination of the tone. The inter-trial interval was variable with an average of 90 sec (+/- 20 sec). Unpaired mice were presented with the same number of CS-rewards and Ensure deliveries, explicitly unpaired from one another and presented in a randomized order. Animals underwent four sessions of reward training (1 session per day). In the second phase of training animals were trained to associate a conditioned stimulus (CS-shock) with a shock delivery. During fear conditioning animals were presented with 30 trials in which a tone cue (3.5 kHz or 20 kHz, counterbalanced, and reversed from the tone pairing used for CS-reward for each mouse) predicted the delivery of a 0.25 sec shock (0.7 mA). The delivery of the shock co-terminated with the predicting tone. ITI was variable with an average of 90 sec (+/- 20 sec). Unpaired mice were presented with the same number of CS-shocks and shock deliveries, explicitly unpaired from one another and presented in a randomized order. Animals underwent two sessions of fear training ('training' and 'test' sessions, 1 session per day). In the second session ('test'), animals were presented with tones only and no shocks.

Following training to recognize each CS, animals were then tested in a two-tone discrimination task. During the discrimination task, animals were presented with 45 CS-reward trials (3.5 kHz or 20 kHz, counterbalanced) and 15 CS-shock trials (20 kHz or 3.5 kHz, counterbalanced), for a total of 60 trials per session. Trials were presented in a pseudorandom manner, and the ITI was variable with an average of 90 sec (+/- 20 sec). Unpaired mice received the same number of CS and US deliveries, explicitly unpaired from one another and presented in a randomized order. Animals underwent discrimination testing for 4-6 sessions (1 session per day) until they achieved 85% reward collection.

For electrophysiology experiments conditioned tones associated with Ensure and shock delivery were 20 seconds in length. Recordings from electrodes were collected continuously throughout the session. For calcium imaging experiments conditioned tones associated with Ensure and shock delivery were 10 seconds in length. For the discrimination task, recordings from miniscopes were collected on select trials (every shock trial, every other reward trial), using a 5V TTL signal to trigger miniscope recordings. Blue LED houselights were also included in the operant chamber to reduce changes in illumination caused by activation of the blue excitation LED from the miniscope. For optogenetic inhibition experiments, conditioned tones associated with Ensure and shock delivery were 20 seconds in length. On a subset of interleaved CS-shock and CS-reward

trials both NpHR and eYFP control mice received laser delivery (593 nm light, 3 mW, constant delivery) beginning 1s prior and ending 1s after the tone on period.

US Experiment

For calcium imaging cohort mice, animals underwent an additional session of US testing to determine responses to both shock and reward when unpredicted by the CS. Over a 45-minute training session, animals experienced foot shock (0.25 sec, 0.7 mA) and Ensure reward (7.5 µL) deliveries of the same magnitude as the discrimination task, presented in a pseudo-random order.

Contextual fear conditioning

For NpHR cohort mice, animals two sessions of contextual fear conditioning over two days. On the first day ('training') mice were placed in a novel environment, allowed to habituate for five minutes, and ten foot shocks (1s, 0.7 mA) were delivered in a randomized order over ten minutes. On the second day ('test day') mice were returned to the environment, and both NpHR and eYFP control mice received laser delivery (593 nm light, 3 mW, constant delivery) during a 10 minute test session, and behavioral responses to conditioned context recorded.

Electrophysiology Recordings

In vivo electrophysiology data acquisition

Electrophysiology data from single-wire probes was recorded using an Open Ephys acquisition board (Siegle et al., 2017) in conjunction with 16 channel Intan headstages (Intan Technologies, Los Angeles, CA). Data was collected at a sampling rate of 30 kHz with a band pass filer to only collect signals between 1 and 7000 Hz.

Neuropixels data acquisition

During behavior, Neuropixels data was acquired using SpikeGLX software (http://billkarsh.github.io/SpikeGLX/) via a National Instruments DAQ (PXIe-1071, PCIe-8381, and PXI-6133) at 30k Hz. Event timestamps were acquired in TTL signals to the National Instruments DAQ at 10k Hz.

Calcium imaging

Calcium imaging data acquisition

UCLA miniscopes V3.2 (http://miniscope.org) were used to collect calcium imaging data (Cai et al., 2016). During behavior, a 5V TTL signal was used to trigger the miniscope recording on select trials. When the scope was triggered, imaging data from the CMOS imaging sensor (Aptina, MT9V032) was transferred to data acquisition (DAQ) electronics and USB Host Controller (Cypress, CYUSB3013) via a co-axial cable. Images were acquired at 15 frames per second at a resolution of 752 X 480 and saved as uncompressed .avi files.

Histology

Following experiments, mice were deeply anaesthetized deeply with sodium pentobarbital (200 mg/kg, intraperitoneal injection). Animals were transcardially perfused with 10 mL of Ringer's solution followed by 10 mL of cold 4% PFA in 1X PBS. Following decapitation and extraction, brains were fixed in 4% PFA in 1X PBS for 24 hrs at 4C. Brains were then transferred to 30% sucrose in 1X PBS at 4C until they sunk to the bottom of the sucrose solution. Brains were sectioned coronally at 50 µm using a microtome (ThermoScientific and were stored at 4C in 1X PBS until staining. Sections were mounted directly onto glass microscope slides and cover slipped with EMS-Shield Mounting Medium w/ DAPI. Slides were then imaged at 10x using the Keyence BZ-X710 Fluorescence microscope. For Neuropixels implants, the trajectory of each Neuropixels probe was reconstructed from brain slices based on The Allen Mouse Brain Common Coordinate Framework (https://www.sciencedirect.com/science/article/pii/S0092867420304025) using Allen CCF tools (https://github.com/cortex-lab/allenCCF).

RNAScope In Situ Hybridization

Preparation of fresh frozen sections for fluorescence in-situ hybridization

8-10 week old C57BL/6J mice from Jackson Laboratories were anesthetized with 5% isoflurane, and brains were immediately extracted and covered with powdered dry ice for 2 minutes, and then stored at -80°C. Brains were then sectioned at 20 µm thick using a cryostat (CM3050 S; Leica, Buffalo Grove, IL) at -16°C. Sections were placed on a glass slide, gently heated from the bottom with the tip of a finger to encourage adhesion of the slice to the slide, and stored at -80°C until further processing.

Fluorescence In-situ hybridization using RNAscope

Fluorescence in-situ hybridization was performed using the Advanced Cell Diagnostics bio V2 RNAScope kit and protocol (Advanced Cell Diagnostics, Newark, CA) using the RNAscope Multiplex Fluorescent Reagent Kit V2 (Catalog #323110), Fluorescent Multiplex Detection Reagents (#323110), probes for *Drd1a* (#406491-C1 and #406491-C3) and *Drd2* (#406501-C3 and #406501-C1), and the Perkin Elmer TSA Plus Fluorescence Palette Kit (NEL760001KT). Fresh frozen slices were fixed in 4% paraformaldehyde for 1 hour at 4°C. Slices were dehydrated in ethanol, and incubated in hydrogen peroxide for 8 minutes, with protease steps omitted to prevent tissue degradation. Slides were incubated in desired probe combinations (*Drd1a* and *Drd2*, which were then counterbalanced for each fluorophore channel) for 2 hours at 40°C. For each channel, slides were incubated in channel-specific HRP for 10 minutes, followed by incubation in TSA fluorophore for 20 minutes, and then incubation in HRP-blocker for 10 minutes. Between all steps, slides were washed 2 times in 1x RNAscope wash buffer for 1-2 minutes. Slides were then incubated in ACDbio DAPI for 10 minutes, washed, dried for 20 minutes, coverslipped with PVA Dabco, and left to dry overnight before imaging.

Confocal microscopy

Confocal fluorescence images were acquired on an Olympus FV1000 confocal laser scanning microscope using a 40x/1.30NA oil immersion objective. Serial Z-stack images were acquired using the FluoView software (Olympus, Center Valley, PA) at a thickness of 1.5 µm per Z stack, with 3-7 planes taken per image. Images were acquired with identical settings for laser power, detector gain, and amplifier offset.

Image Processing

Images were opened in ImageJ and individual Z-planes encompassing the entire ROI were selected from each image for further image processing. Background was subtracted from all channels in all images using the subtract background feature in ImageJ. Each channel was then further thresholded using the brightness and contrast feature in ImageJ. Thresholds were determined by manually thresholding 10 images to a level with no background, and then computing the average minimum threshold necessary to remove background. The average threshold across 10 images was then used as the threshold for all images. Masks of each region were drawn based on the mouse brain atlas (Paxinos and Franklin, 2004) Images were then saved as 8bit TIFFs for further cell and puncta identification in CellProfiler.

Single-nucleus RNA sequencing:

Tissue extraction and cryopreservation

All procedures were performed in accordance with Institutional Animal Care and Use Committee protocol S16054 at the University of California, San Diego. All mice in the study were wild-type C57BL/6J background and received directly from Jackson Laboratories at 6 weeks of age and acclimated to the colony prior to experiments. Animals were single-housed and maintained free from noise or disturbance for 24 hours prior to sacrifice to reduce artifactual immediate early gene expression. Sacrifice was performed at P60 ± 3 days (n = 10-15 mice per pool for ASt, 10 for CeA, 9-10 for tail of striatum, 5 for body of striatum). Sample size was determined based on amount of expected nuclei per region per mouse: estimates of expected nuclei were determined empirically, though nuclear recovery was approximately 20% of total based on cellular density estimates from the Blue Brain Cell Atlas. 12,000 nuclei were targeted per combination of assay, condition, and region, which was determined using Single-Cell One-sided Probability Interactive Tool (SCOPIT) v1.1.4, allowing potential detection of at least 5 nuclei from 10 rare subpopulations at 0.1% frequency with 95%

probability (Davis et al., 2019). All sacrifices were performed during the dark period of the light cycle. Animals were anesthetized via combined intraperitoneal injection of 150 mg/kg ketamine and 15 mg/kg xylazine. Once unconscious, mice animals were transcardially perfused with ice-cold, carbogen-bubbled (95% O_2, 5% CO_2), nuclease-free, 0.22 µm sterile-filtered artificial cerebrospinal fluid (ACSF) with a composition of 93 mM *N*-methyl-*D*-glucamine, 2.5 mM KCl, 1.2 mM NaH_2PO_4, 30 mM $NaHCO_3$, 20 mM HEPES, 25 mM glucose, 5 mM sodium ascorbate, 2 mM thiourea, 3 mM sodium pyruvate, 13.2 mM trehalose, 12 mM *N*-acetyl-cysteine, 0.5 mM $CaCl_2$, 10 mM $MgSO_4$, and 93 mM HCl, at pH 7.3-7.4.(Tasic et al., 2018; Ting et al., 2014) Following transcardial perfusion, brains were immediately extracted and submerged into ice-cold carbogen-bubbled ACSF, with less than 5 minutes between the beginning of perfusion and final submersion after extraction. Brains were serially sectioned in ice-cold, carbogen-bubbled ACSF on a VT1000S vibratome (Leica) with polytetrafluoroethane-coated razor blades (Ted Pella) at 0.15 mm/sec and 100 Hz, dividing the whole cerebrum into 400 µm coronal slices. Target regions were microdissected from these slices under a stereomicroscope using a sterile blunt-end needle (22 gauge for CeA, ASt, and tail of striatum, 16 gauge for dorsal striatum). All regions were targeted using *Paxinos and Franklin's the Mouse Brain in Stereotaxic Coordinates* as reference (Paxinos and Franklin, 2019). Extracted tissue samples were recovered in ice-cold, nuclease-free, 0.22 µm sterile-filtered cryoprotective nuclear storage buffer, composed of 0.32 M sucrose, 5 mM $CaCl_2$, 3 mM magnesium acetate, 10 mM Trizma hydrochloride buffer (pH 8.0), 1 mM dithiothreitol, 0.02 U/µl SUPERase•In RNAse Inhibitor (Invitrogen), and 1X cOmplete Protease Inhibitor Cocktail with EDTA (Roche). Tissue was then snap frozen using a metal CoolRack M90 (Biocision) pre-chilled to -80˚C and stored at -80˚C until nuclear isolation. Following extraction of tissue regions of interest, remaining portions of sections were fixed in 4% paraformaldehyde and 4′,6-diamidino-2-phenylindole (DAPI) was applied to sections at 1 µg/ml. After fixation and staining, sections were mounted and imaged on an VS120 slide scanner (Olympus). From these images, dissection accuracy was assessed for each region, and individual samples were only selected for downstream nuclear isolation if the extracted tissue fell entirely within the defined target regions.

Nuclear isolation and sorting

Nuclear isolation procedures were adapted from multiple methods described previously.(Krishnaswami et al., 2016; Preissl et al., 2018) All procedures were performed on ice, and all solutions were ice-cold, nuclease-free, and 0.22 µm sterile-filtered. Cryopreserved tissue pieces were slow-thawed by incubation at 4˚C for 1 hour prior to isolation. Tissue pieces were then pooled and resuspended in nuclear isolation medium composed of 0.25 M sucrose, 25 mM KCl, 5 mM $MgCl_2$, 10 mM Trizma hydrochloride buffer (pH 7.4), 1 mM dithiothreitol, 0.04 U/µl RNasin Plus RNAse Inhibitor (Promega), 1X cOmplete Protease Inhibitor Cocktail with EDTA (Roche), and 0.1% Triton-X. The pooled tissue pieces in nuclear isolation medium were transferred to a 2 mL Dounce tissue grinder. Tissue was homogenized by 5 strokes from the loose pestle and 15 followed by the tight pestle, and the resulting homogenate was filtered through a 40 µm Flowmi cell strainer (Bel-Art) into a 1.5 ml Lo-Bind tube (Eppendorf). The homogenate was then centrifuged with a swinging bucket rotor at 4˚C and 1000 x g for 8 minutes. Nuclei were then washed with nuclear flow buffer composed of DPBS with 1% bovine serum albumin, 1 mM dithiothreitol, and 0.04 U/µl RNAsin Plus RNAse Inhibitor (Promega) and centrifuged at 4˚C and 500 x g for 5 minutes, which was subsequently repeated. Nuclei were finally resuspended in nuclear flow buffer containing 3 µm DRAQ7 (Cell Signaling Technology) and again filtered through a 40 µm Flowmi cell strainer into a 5 ml round-bottom polystyrene tube. Each isolation took under 45 minutes to perform, from homogenization to final suspension.

Fluorescence-activated nuclei sorting (FANS) was carried out on a FACSAria II SORP (BD Biosciences) using a 70 µm nozzle at 52 PSI sheath pressure. For FANS, debris was first excluded by gating on forward and side scatter pulse area parameters (FSC-A and SSC-A), followed by exclusion of aggregates (FSC-W and SSC-W), and finally gating for nuclei based on DRAQ7 fluorescence (FSC-A and APC-Cy7-A). Only the set of DRAQ7+ nuclei at the first level of fluorescence were sorted to enrich for singlets, given stoichiometric DNA binding. Nuclei were successively sorted into 1.5 ml LoBind tubes (Eppendorf) under the purity sort mode. The tube contained 10X RT master mix without RT Buffer C. 16,000 total nuclei were targeted for downstream processing, and to account for cytometer errors and subsequent loss of nuclei, up to 21,000 detected nuclei were sorted into the tube to yield 16,000 viable nuclei for downstream sequencing (if fewer than 21,000 nuclei were detected, all were sorted into the tube). Nuclei were then immediately processed for snRNA-seq.

Library preparation and sequencing

Nuclear suspensions were converted into barcoded snRNA-seq libraries using the Chromium Next GEM Single Cell 3' v3.1 Reagent Kits v3.1 Single Index (10X Genomics). Library preparation for both assays was performed in accordance with the manufacturer's instructions. 10,000 nuclei were targeted during each snRNA-seq library preparation run, and each region was performed in duplicate at minimum (*n* = 2 libraries for ASt, 3 for CeA and tail of striatum, 4 for body of striatum).

10X libraries were first sequenced at low depth on a NextSeq 550 Sequencing System (Illumina) to estimate quality and number of nuclei for each library, followed by deep sequencing on a NovaSeq 6000 Sequencing System. All runs were performed using 2 x 100-bp paired-end reads, outputting data in 28/8/91-bp read format. All sequences were demultiplexed using bcl2fastq.

QUANTIFICATION AND STATISTICAL ANALYSIS

Statistical Analysis

Statistical analyses were performed using either GraphPad Prism (GraphPad Software, Inc, La Jolla, CA, USA) or MATLAB (Mathworks, Natick, MA, USA). Group comparisons were made using either one-way or two-way analysis of variance (ANOVA) followed by Bonferroni post hoc tests. Non-parametric Wilcoxon signed-rank tests were used to compare in vivo neural firing rates across conditions, using an a = 0.01. An a = 0.01 was also used to determine whether z-score transformed peri-stimulus time histograms of neural data exhibited significant neural responses. Multiple comparisons were corrected when appropriate by adjusting P values using the Bonferroni method. The number of animals (N) and the number of neurons (n) recorded is specified in the figures, the figure legends, and the text.

Statistical Analysis of Behavior

Behavioral Analysis of Open Field Test, Elevated Plus Maze, and Real-Time Place Preference

Behavioral performance was recorded by digital cameras positioned above the test arena. Ethovision XT software (Noldus, Wagenigen, Netherlands) was used to track mouse location

Behavioral Analysis of Two-tone Discrimination Task

To automatically detect animal defensive behaviors, SLEAP (Pereira et al., 2022) was used to estimate animal poses in behavioral videos. A training data set of over 6000 frames was labeled using a 14-point skeleton to represent the mouse (nose, left ear tip, left ear base, right ear base, right ear tip, skull base, shoulders, haunch, tail base, tail segment, left arm, right arm, right leg, and left leg). This data set was used to train a top-down model; in this model, first the animal is detected using a centroid model, then the location of each labeled body part is identified using a centered instance model. To identify times when an animal was freezing, the total sum of distance travelled of each body point between the current and previous frames had to surpass a freezing-threshold. To detect escape behavior, the distance traveled of the haunch point in the current and previous frame compared to a dashing-threshold was examined. Thresholds were set for each experiment by visual inspection to ensure the automatically detected freeze and escape frames aligned with the animal's true behavior, and 'total defensive behaviors' was calculated as the sum of freezing or escape behaviors. To detect reward seeking behavior, port entries and exits were determined from reward port infrared beam breaks (Med-PC IV, Med Associates).

Statistical Analysis of Electrophysiology Recordings

Neuropixel Recordings

Acquired data were prepossessed using CatGT (https://billkarsh.github.io/SpikeGLX/#catgt). Preprocessed data were then sorted into spike clusters using Kilosort 2.5 (https://github.com/MouseLand/Kilosort), which provides a drift-tracking feature that detects the footprints of the same neuron during a recording session while correcting for drift. To determine the quality metrics of sorted spike clusters, we used modules for processing extracellular electrophysiology data provided by the Allen Institute. All tools described above were combined in

Python using custom-written scripts (https://github.com/jenniferColonell/ecephys_spike_sorting). Finally, manual curation was performed to identify individual neurons and to remove multiunit and noise clusters using phy (https://phy.readthedocs.io/en/latest/).

In vivo Electrophysiology Recordings

Preparation of files for cluster sorting was carried out using a custom MATLAB algorithm. Spikes were thresholded to a 6 sigma criteria and traces were aligned to their depolarization peak. Spikes were exported in a .plx file format to be imported into Offline Sorter (Plexon Inc., Dallas TX). Once spikes were imported, principal component analysis was used to cluster spikes into individual units.

Analysis of neural responses to cue delivery

For all electrophysiology experiments, to calculate the neuronal response to each conditioned stimulus, the mean activity for each neuron across all trials of a given trial type was calculated and Z-score of changes in firing rate was calculated based on mean and standard deviation for that neuron during a 20 second baseline period immediately preceding the onset of the cue. For hierarchical clustering, each neuron's Z-score response for reward trials and fear trials were horizontally concatenated then clustered using agglomerative hierarchical clustering based on Euclidean distance with a custom MATLAB script. For 'phasic' and 'sustained' responses, the mean Z-score was calculated during a period of 1ms-100 ms following the cue and 100ms to 18s following the cue, respectively.

Neural Trajectory Analysis

To visualize the population-level firing rate dynamics, a single global Principal Component Analysis (PCA) was applied to a matrix containing the standardized, trial-averaged neural activity (concatenated activity during shock and reward trials) of all animals (paired and unpaired). This enabled the comparison of the neural trajectories across the experimental groups. The mean firing rate for each group of animals and each trial type was then projected into this principal component space and their trajectories within the first three dimensions are shown. The distance between the shock and reward trajectories for each experimental group was calculated as the Euclidean distance within each time-bin using the complete principal component space. For the visualization, we smoothed each trajectory by convolving the signal with a one-directional Gaussian.

Logistic regression classifier

To test whether ASt neural activity within a trial is correlated with various behavioral variables logistic regression models were used (Glaser et al., 2020). For each mouse separately, the neural activity of all trials was divided into five non overlapping folds to use for cross-validation. To classify whether CS-shock or CS-reward was presented during a trial, a logistic regression classifier was trained on the training folds and evaluated time-bin by time-bin on the held-out trials. Similarly, separate classifiers were trained to decode whether the mouse was engaging in freezing or escape behavior. The training data was balanced to ensure there were an equal number of time points for each class.

Statistical Analysis of Calcium Recordings

Imaging data was then concatenated and temporally downsampled by a factor of two using a custom MATLAB script before motion correction (rigid registration) via the NoRMCorre algorithm (Pnevmatikakis and Giovannucci, 2017). Neuron detection and signal extraction was done using the CNMF-E algorithm (Zhou et al., 2018). Using a MATLAB Neuron Deletion GUI, neurons exhibiting abnormalities in morphology and calcium trace were manually excluded. Neuron curation was performed by experimenters blinded to the experimental condition.

Analysis of neural responses to cue delivery

To calculate the neuronal response to each conditioned stimulus, the mean GCaMP7f fluorescence for each neuron across trials for each trial type was calculated, and Z-score of fluorescence values calculated based on mean and standard deviation for that neuron during a 10 second baseline period immediately preceding the onset of the cue. For clustering, each neuron's individual Z-score response for CS-shock trials and CS-reward trials were horizontally concatenated using a custom MATLAB script and clustered using agglomerative hierarchical clustering based on Euclidean distance, with soft normalization of neurons to a maximum Z-score

of 10. For the US-only experiment, Z-scores were calculated for each neuron based on a 5 second baseline period immediately preceding shock delivery or consumption of reward.

Statistical Analysis of RNAScope In Situ Hybridization

Object Identification and analysis

Image TIFFs were run through CellProfiler using an optimized version of the CellProfiler Colocalization pipeline (https://cellprofiler.org/examples/). The pipeline was optimized to identify DAPI labelled cells (18-45 pixels in diameter) and then subsequently identify mRNA puncta (4-10 pixels in diameter). DAPI cell detection was further restricted by shrinking DAPI ROIs by 1 pixel. Puncta overlapping with DAPI-identified cells (using the relate objects module) were considered for analysis to assess the level of mRNA expression per cell. To determine if cells were expressing mRNA, a threshold of 5 or more puncta within twice the diameter of nucleus centered over the nucleus was used (McCullough et al., 2018). Total number and density of *Drd1a*+ and *Drd2*+ cells in each region of interest were calculated from CellProfiler .csv outputs using custom MATLAB code.

Statistical Analysis of Single-nucleus RNA sequencing

Sequence alignment

All samples were processed using CellRanger (v5.0.0) (Zheng et al., 2017). All processing was done by using CellRanger's implementation of STAR to align sample sequence reads to their pre-built mm10 vm23/Ens98 reference transcriptome index 2020-A, with predicted and non-validated transcripts removed. All sequencing reads were aligned to both the exons and the introns present in the index. Samples were demultiplexed to produce a pair of FASTQ files for each sample. FASTQ files containing raw read sequence information were aligned to the CellRanger index using the cellranger count command with --chemistry SC3Pv3 and --include-introns flags enabled. CellRanger corrected sequencing errors in cell barcodes to pre-defined sequences in the 10X v3 single-index whitelist within Hamming distance 1. PCR duplicates were removed by selecting unique combinations of corrected cell barcodes, unique molecular identifiers, gene names, and location within the transcript. Raw unfiltered count data was read into R (v4.0.3) using the Seurat package (v4.0) (Butler et al., 2018; Hao et al., 2021; Satija et al., 2015; Stuart et al., 2019).The final result of the pipeline was a barcode x gene expression matrix for further analysis downstream.

Quality control

We used the raw, unfiltered matrix output from CellRanger as the input to the beginning of the pipeline. However, to apply a more stringent filter, the emptyDrops dirichlet-multinomial model from the DropletUtils package (v1.10.2) was applied to each library individually (Griffiths et al., 2018; Lun et al., 2019). Droplets with less than 100 total counts were used to construct the ambient RNA profile and an FDR threshold below 0.001 was used to select putatively occupied droplets. All barcodes with greater than 1000 UMIs were further assumed non-empty. Most quality filtration choices were heavily influenced by the recommendations presented in pipeComp (Germain et al., 2020). All quality control was performed on each library individually prior to merging. Minimal quality filtering for each barcode was performed by setting a floor of 1000 features per barcode for downstream inclusion to ensure the dataset is entirely composed of high-quality nuclei. Next, to remove highly likely multiplet barcodes, barcodes were filtered out if their count depth was more than 5 median absolute deviations above the median count depth. Barcodes were then removed if their proportion of ribosomal or mitochondrial reads was more than 5 interquartile ranges above the 75th percentile. Heterotypic doublets were identified by creating simulated artificial doublets in scDblFinder (v1.4.1), which uses a DoubletFinder-like model to remove barcodes similar to simulated doublets, with an assumed doublet rate of 1% per 1000 nuclei in the library (Germain and Lun, 2021; McGinnis et al., 2019). Scater (v1.18.3) was used to produce initial diagnostic tSNE and UMAP plots for visually checking the influence of each above metric on the structure of the data (McCarthy et al., 2017). Downstream, one cluster of diffusely-distributed neurons with few marker genes and disproportionately low read depth and disproportionately high mitochondrial and ribosomal gene proportions was removed as low-quality cells.

Data processing/transformation.

All datasets (initially for all nuclei and again for selected subclusters) were formatted into Seurat objects (v4.0.0), merged, and then normalized and transformed individually using the SCTransform (v2) variance

stabilizing transform, which performs best according to prior comparisons in pipeComp (Choudhary and Satija, 2022; Germain et al., 2020; Hafemeister and Satija, 2019). Following the merge, all genes expressed in 3 or fewer cells were removed from analysis. SCTransform was run returning Pearson residuals regressing out mitochondrial gene expression, first with 5000 highly variable features, and then with 3000 for subsequent iterations on subsets of the data. Dimensionality of the dataset was first reduced using principal component analysis, as implemented in Seurat's RunPCA function (Jolliffe and Cadima, 2016). The top 50 principal components were retained for downstream analysis. These principal components (top 25 for all nuclei, top 15 for subclusters) were used as input to the non-linear tSNE and UMAP dimensionality reduction methods as implemented by Seurat's RunTSNE and/or RunUMAP functions (n.epochs = 1000, min.dist = 0.5) at default settings unless otherwise specified (Becht et al., 2019; Maaten and Hinton, 2008; McInnes et al., 2018).

Differential expression

Marker genes were identified using Wilcoxon rank-sum test as implemented by the FindConservedMarkers function in Seurat, using the region as a grouping variable. Genes were accepted as differentially expressed with a minimum proportion cutoff at 0.1 and minimum fold change at 1.5-fold (log2-fold change of 0.585), with a p-value cutoff of 0.01 after Bonferroni correction. To identify genes differentially expressed by region, single-cell values were converted to pseudo-bulk by batch using the run_de function as implemented in the Libra package (v1.0.0) using default settings, and tested for differential expression using edgeR's likelihood ratio test (Robinson et al., 2010; Squair et al., 2021). Region-specific genes were identified by comparing batches from one region to all others, while pairwise differentially-expressed genes were identified between batches from just the two regions of interest, and genes were retained with a minimum fold change at 1.5-fold (log2-fold change of 0.585), at a p-value cutoff of 0.01 after Benjamini-Hochberg correction. Neurologically-related genes of interest were determined by filtering region-specific differentially expressed genes through a subset of pre-selected gene families from HGNC with known functions related to neural structure and function (Tweedie et al., 2021).

METHODS REFERENCES:

Becht, E., McInnes, L., Healy, J., Dutertre, C.-A., Kwok, I.W.H., Ng, L.G., Ginhoux, F., Newell, E.W., 2019. Dimensionality reduction for visualizing single-cell data using UMAP. Nat Biotechnol 37, 38–44. https://doi.org/10.1038/nbt.4314

Butler, A., Hoffman, P., Smibert, P., Papalexi, E., Satija, R., 2018. Integrating single-cell transcriptomic data across different conditions, technologies, and species. Nature Biotechnology 36, 411–420. https://doi.org/10/gc87v6

Cai, D.J., Aharoni, D., Shuman, T., Shobe, J., Biane, J., Song, W., Wei, B., Veshkini, M., La-Vu, M., Lou, J., Flores, S.E., Kim, I., Sano, Y., Zhou, M., Baumgaertel, K., Lavi, A., Kamata, M., Tuszynski, M., Mayford, M., Golshani, P., Silva, A.J., 2016. A shared neural ensemble links distinct contextual memories encoded close in time. Nature 534, 115–118. https://doi.org/10.1038/nature17955

Choudhary, S., Satija, R., 2022. Comparison and evaluation of statistical error models for scRNA-seq. Genome Biology 23, 27. https://doi.org/10.1186/s13059-021-02584-9

Davis, A., Gao, R., Navin, N.E., 2019. SCOPIT: sample size calculations for single-cell sequencing experiments. BMC Bioinformatics 20, 566. https://doi.org/10/ggc9ws

Germain, P.-L., Lun, A., 2021. scDblFinder: scDblFinder. Bioconductor version: Release (3.12). https://doi.org/10.18129/B9.bioc.scDblFinder

Germain, P.-L., Sonrel, A., Robinson, M.D., 2020. pipeComp, a general framework for the evaluation of computational pipelines, reveals performant single cell RNA-seq preprocessing tools. Genome Biology 21, 227. https://doi.org/10/ghb3tq

Griffiths, J.A., Richard, A.C., Bach, K., Lun, A.T.L., Marioni, J.C., 2018. Detection and removal of barcode swapping in single-cell RNA-seq data. Nat Commun 9. https://doi.org/10/gdw373

Hafemeister, C., Satija, R., 2019. Normalization and variance stabilization of single-cell RNA-seq data using regularized negative binomial regression. Genome Biology 20, 296. https://doi.org/10.1186/s13059-019-1874-1

Hao, Y., Hao, S., Andersen-Nissen, E., Mauck, W.M., Zheng, S., Butler, A., Lee, M.J., Wilk, A.J., Darby, C., Zager, M., Hoffman, P., Stoeckius, M., Papalexi, E., Mimitou, E.P., Jain, J., Srivastava, A., Stuart, T., Fleming, L.M., Yeung, B., Rogers, A.J., McElrath, J.M., Blish, C.A., Gottardo, R., Smibert, P., Satija, R., 2021. Integrated analysis of multimodal single-cell data. Cell 184, 3573-3587.e29. https://doi.org/10.1016/j.cell.2021.04.048

Jolliffe, I.T., Cadima, J., 2016. Principal component analysis: a review and recent developments. Philosophical Transactions of the Royal Society A: Mathematical, Physical and Engineering Sciences 374, 20150202. https://doi.org/10.1098/rsta.2015.0202

Krishnaswami, S.R., Grindberg, R.V., Novotny, M., Venepally, P., Lacar, B., Bhutani, K., Linker, S.B., Pham, S., Erwin, J.A., Miller, J.A., Hodge, R., McCarthy, J.K., Kelder, M., McCorrison, J., Aevermann, B.D., Fuertes, F.D.,

Scheuermann, R.H., Lee, J., Lein, E.S., Schork, N., McConnell, M.J., Gage, F.H., Lasken, R.S., 2016. Using single nuclei for RNA-seq to capture the transcriptome of postmortem neurons. Nat Protoc 11, 499–524. https://doi.org/10/f8d3qc

Lun, A.T.L., Riesenfeld, S., Andrews, T., Dao, T.P., Gomes, T., Marioni, J.C., participants in the 1st Human Cell Atlas Jamboree, 2019. EmptyDrops: distinguishing cells from empty droplets in droplet-based single-cell RNA sequencing data. Genome Biology 20, 63. https://doi.org/10/gfxdhf

Maaten, L. van der, Hinton, G., 2008. Visualizing Data using t-SNE. Journal of Machine Learning Research 9, 2579–2605.

McCarthy, D.J., Campbell, K.R., Lun, A.T.L., Wills, Q.F., Hofacker, I., 2017. Scater: pre-processing, quality control, normalization and visualization of single-cell RNA-seq data in R. Bioinformatics 33, btw777. https://doi.org/10/gfgp3m

McCullough, K.M., Daskalakis, N.P., Gafford, G., Morrison, F.G., Ressler, K.J., 2018. Cell-type-specific interrogation of CeA Drd2 neurons to identify targets for pharmacological modulation of fear extinction. Transl Psychiatry 8, 1–16. https://doi.org/10.1038/s41398-018-0190-y

McGinnis, C.S., Murrow, L.M., Gartner, Z.J., 2019. DoubletFinder: Doublet Detection in Single-Cell RNA Sequencing Data Using Artificial Nearest Neighbors. Cell Syst 8, 329-337.e4. https://doi.org/10/gg5m57

McInnes, L., Healy, J., Melville, J., 2018. UMAP: Uniform Manifold Approximation and Projection for Dimension Reduction. arXiv:1802.03426 [cs, stat].

Paxinos, G., Franklin, K.B.J., 2019. Paxinos and Franklin's the Mouse Brain in Stereotaxic Coordinates. Academic Press.

Pereira, T.D., Tabris, N., Matsliah, A., Turner, D.M., Li, J., Ravindranath, S., Papadoyannis, E.S., Normand, E., Deutsch, D.S., Wang, Z.Y., McKenzie-Smith, G.C., Mitelut, C.C., Castro, M.D., D'Uva, J., Kislin, M., Sanes, D.H., Kocher, S.D., Wang, S.S.-H., Falkner, A.L., Shaevitz, J.W., Murthy, M., 2022. SLEAP: A deep learning system for multi-animal pose tracking. Nat Methods 19, 486–495. https://doi.org/10.1038/s41592-022-01426-1

Pnevmatikakis, E.A., Giovannucci, A., 2017. NoRMCorre: An online algorithm for piecewise rigid motion correction of calcium imaging data. Journal of Neuroscience Methods 291, 83–94. https://doi.org/10.1016/j.jneumeth.2017.07.031

Preissl, S., Fang, R., Huang, H., Zhao, Y., Raviram, R., Gorkin, D.U., Zhang, Y., Sos, B.C., Afzal, V., Dickel, D.E., Kuan, S., Visel, A., Pennacchio, L.A., Zhang, K., Ren, B., 2018. Single-nucleus analysis of accessible chromatin in developing mouse forebrain reveals cell-type-specific transcriptional regulation. Nat. Neurosci. 21, 432–439. https://doi.org/10/gc9gx2

Robinson, M.D., McCarthy, D.J., Smyth, G.K., 2010. edgeR: a Bioconductor package for differential expression analysis of digital gene expression data. Bioinformatics 26, 139. https://doi.org/10.1093/bioinformatics/btp616

Satija, R., Farrell, J.A., Gennert, D., Schier, A.F., Regev, A., 2015. Spatial reconstruction of single-cell gene expression data. Nature Biotechnology 33, 495–502. https://doi.org/10.1038/NBT.3192

Siegle, J.H., López, A.C., Patel, Y.A., Abramov, K., Ohayon, S., Voigts, J., 2017. Open Ephys: an open-source, plugin-based platform for multichannel electrophysiology. J Neural Eng 14, 045003. https://doi.org/10.1088/1741-2552/aa5eea

Squair, J.W., Gautier, M., Kathe, C., Anderson, M.A., James, N.D., Hutson, T.H., Hudelle, R., Qaiser, T., Matson, K.J.E., Barraud, Q., Levine, A.J., La Manno, G., Skinnider, M.A., Courtine, G., 2021. Confronting false discoveries in single-cell differential expression. Nat Commun 12, 5692. https://doi.org/10.1038/s41467-021-25960-2

Stuart, T., Butler, A., Hoffman, P., Hafemeister, C., Papalexi, E., Mauck, W.M., Hao, Y., Stoeckius, M., Smibert, P., Satija, R., 2019. Comprehensive Integration of Single-Cell Data. Cell 177, 1888-1902.e21. https://doi.org/10.1016/j.cell.2019.05.031

Tasic, B., Yao, Z., Graybuck, L.T., Smith, K.A., Nguyen, T.N., Bertagnolli, D., Goldy, J., Garren, E., Economo, M.N., Viswanathan, S., Penn, O., Bakken, T., Menon, V., Miller, J., Fong, O., Hirokawa, K.E., Lathia, K., Rimorin, C., Tieu, M., Larsen, R., Casper, T., Barkan, E., Kroll, M., Parry, S., Shapovalova, N.V., Hirschstein, D., Pendergraft, J., Sullivan, H.A., Kim, T.K., Szafer, A., Dee, N., Groblewski, P., Wickersham, I., Cetin, A., Harris, J.A., Levi, B.P., Sunkin, S.M., Madisen, L., Daigle, T.L., Looger, L., Bernard, A., Phillips, J., Lein, E., Hawrylycz, M., Svoboda, K., Jones, A.R., Koch, C., Zeng, H., 2018. Shared and distinct transcriptomic cell types across neocortical areas. Nature 563, 72. https://doi.org/10/gfgqmf

Ting, J.T., Daigle, T.L., Chen, Q., Feng, G., 2014. Acute brain slice methods for adult and aging animals: application of targeted patch clamp analysis and optogenetics. Methods Mol. Biol. 1183, 221–242. https://doi.org/10/ggc92j

Tweedie, S., Braschi, B., Gray, K., Jones, T.E.M., Seal, R.L., Yates, B., Bruford, E.A., 2021. Genenames.org: the HGNC and VGNC resources in 2021. Nucleic Acids Res 49, D939–D946. https://doi.org/10.1093/nar/gkaa980

Zheng, G.X.Y., Terry, J.M., Belgrader, P., Ryvkin, P., Bent, Z.W., Wilson, R., Ziraldo, S.B., Wheeler, T.D., McDermott, G.P., Zhu, J., Gregory, M.T., Shuga, J., Montesclaros, L., Underwood, J.G., Masquelier, D.A., Nishimura, S.Y., Schnall-Levin, M., Wyatt, P.W., Hindson, C.M., Bharadwaj, R., Wong, A., Ness, K.D., Beppu, L.W., Deeg, H.J., McFarland, C., Loeb, K.R., Valente, W.J., Ericson, N.G., Stevens, E.A., Radich, J.P., Mikkelsen, T.S., Hindson, B.J., Bielas, J.H., 2017. Massively parallel digital transcriptional profiling of single cells. Nature Communications 8, 14049. https://doi.org/10/f9mbtp

Zhou, P., Resendez, S.L., Rodriguez-Romaguera, J., Jimenez, J.C., Neufeld, S.Q., Giovannucci, A., Friedrich, J., Pnevmatikakis, E.A., Stuber, G.D., Hen, R., Kheirbek, M.A., Sabatini, B.L., Kass, R.E., Paninski, L., 2018.

Efficient and accurate extraction of in vivo calcium signals from microendoscopic video data. eLife 7, e28728. https://doi.org/10.7554/eLife.28728

REAGENT or RESOURCE	SOURCE	IDENTIFIER
Bacterial and virus strains		
AAV5-EF1a-DIO-eYFP	UNC Vector Core	# 4310B
AAV5-EF1a-DIO-hChR2(H134R)-eYFP	UNC Vector Core	# AV4313-2A
AAV5-EF1a-DIO-eNpHR3.0-eYFP	UNC Vector Core	# 4806
AAV1-syn-FLEX-jGCaMP7f-WPRE	Addgene	# v49556
Biological samples		
Chemicals, peptides, and recombinant proteins		
‘	ACDBio	406491
RNAscope® Probe- Mm-Drd2	ACDBio	406501
RNAscope® Probe- Mm-Drd1a-C3	ACDBio	406491-C3
RNAscope® Probe- Mm-Drd2-C3	ACDBio	406501-C3
RNAscope® Multiplex Fluorescent Reagent Kit v2	ACDBio	323100
Dapi-Fluoromount-G™	Electron Microscopy Sciences	17984-24
PVA-DABCO	Sigma-Aldrich	Cat# 10981-100ml
"C" Universal TBB Catalyst	Parkell	S396
Radiopaque L-Powder for C&B-METABOND®	Parkell	S396
"B" Quick Base For C&B METABOND®	Parkell	S398
Ortho-Jet Powder (Black)	Lang Dental	1330CLR
Ortho-Jet™ Liquid	Lang Dental	1304CLR
Critical commercial assays		
Deposited data		
Single nucleus RNA-seq data		GEO: GSE211437
Experimental models: Organisms/strains		
Mouse: wild-type C57BL6J	Jackson Laboratory	RRID:IMSR_JAX:000664
Mouse: B6.FVB(Cg)-Tg(Drd1-cre)EY262Gsat/Mmucd	MMRRC	RRID:MMRRC_036089-UCD
Mouse: B6.FVB(Cg)-Tg(Drd2-cre)ER44Gsat/Mmucd	Jackson Laboratory	RRID:MMRRC_036089-UCD
Mouse: B6J.129S6(FVB)-Slc32a1tm2(cre)Lowl/MwarJ	Jackson Laboratory	RRID:IMSR_JAX:028862

Software and algorithms		
Prism 6	Graphpad	https://www.graphpad.com/
MATLAB R2018a	Mathworks	https://www.mathworks.com/
Ethovision XT	Noldus	http://www.noldus.com/animal-behavior-research/products/ethovision-xt
SLEAP	Pereira et al., 2022	https://sleap.ai/
Other		
Fibers for Optogenetics	RWD	Cat# 907-03020-00
Ferrules for optogenetics	Kientec Systems	Cat# FSS-LC-330
Conditioning Chambers	Med Associates INC	http://www.med-associates.com/products/; Number: ENV-008
Behavioral Chambers (3-Chamber, Open Field, Elevated Plus Maze)	California Model and Design	http://www.anyscale.com/#/scientific/
Small animal stereotax	David Kopf Instruments	http://kopfinstruments.com/product/model-942-small-animal-stereotaxic-instrument-with-digital-display-console/
Microscope BX51 for ex vivo recordings	Olympus	Discontinued product
P-1000 Horizontal puller for glass microelectrodes for ex vivo recordings	Sutter	https://www.sutter.com/MICROPIPETTE/
HM430 sliding microtome	Thermo Fisher Scientific	Cat# 910010
STABLOHM 675	California Fine Wire Company	#: 100188
0.5 x 6.1mm GRIN Lens Probe	Inscopix Inc.	1050-004599
1.8mm Dia, 670nm DWL, 0.0mm WD, Uncoated, GRIN Lens	Edmund Optics	64519
Miniscope V3.2 Body	miniscopeparts	https://miniscopeparts.com/products/ols/categories/v3
Miniscope V3.2 baseplate	miniscopeparts	https://miniscopeparts.com/products/ols/categories/v3
V3.2 Base Plate Cap	miniscopeparts	https://miniscopeparts.com/products/ols/products/v32baseplatecap

3.0mm Diameter, N-BK7 Half-Ball Lens	Edmund Optics	47-269
Diced dichroic mirror, 6mm x 4mm x 1mm	Chroma	T495lpxr
Diced emission filter, 4mm x 4mm x 1mm	Chroma	ET525/50m
5mm Dia. x 7.5mm FL, MgF2 Coated, Achromatic Doublet Lens	Edmund Optics	45-407
Flexible wire for connecting LED and imaging sensor PCBs	McMaster Carr	9510T2
Coaxial Cables 42AWG PFA, 50 OHM MICRO COAX, PER FT	Mouser	538-50MCX-37
Excitation LED, LED LUXEON REBEL BLUE SMD	Digikey	LXML-PB01-0030
Aptina (OnSemiconductor) monchromatic CMOS imaging sensor	Arrow Electronis or Aliexpress	Discontinued product
4 layer, 0.031" CMOS imaging sensor PCB	LabMaker	Discontinued product
2 layer, 0.031" Excitation LED PCB	Silver Circuits	
2 layer, 0.062" Coax to SMA PCB	OSH Park	
1/16" diameter x 1/32" thick. Axially Magnetized	K&J Magnetics, Inc.	D101-N52
Set Screw 18-8 Stainless Steel Cup Point Set Screw, 0-80 Thread, 3/16" Long	McMaster Carr	92311A054